LATVIJAS UNIVERSITĀTE
FIZIKAS UN MATEMĀTIKAS FAKULTĀTE

Andris Bērziņš

Magnetooptiskie efekti sārmu metālu tvaikos un to pielietojumi magnētiskā lauka mērījumos

---

Magnetooptical effects in alkali metal vapour and their applications in magnetic field measurements

Zinātnisko publikāciju kopa

Doktora grāda iegūšanai fizikas nozarē
Apakšnozare: lāzeru fizika un spektroskopija

Scientific paper collection

Submitted for the Doctoral Degree in Physics
Subfield: Laser Physics and Spectroscopy

Darba vadītājs (Supervisor): Dr. hab. phys. Ruvins Ferbers

Rīga, 2016

Anotācija

Promocijas darbs veltīts tumšo un gaišo magnetooptisko rezonanšu eksperimentālai izpētei.

Izmantojot eksperimentālos rezultātus D_2 līnijas pārejām ^{85}Rb un ^{87}Rb, pirmo reizi izskaidrota gaišās magnetooptiskās rezonanses pārvēršanās par tumšo, mainoties lāzera jaudas blīvumam pie fiksētas lāzera frekvences.

Izmantojot eksperimentālos rezultātus, kas iegūti lietojot ļoti plāno šūnu un Cs D_1 līnijas pārejas, uzlabots sadursmju relaksāciju un caurlidošanas relaksācijas apraksts.

Izmantojot ļoti plāno šūnu un Cs D_1 līnijas pārejas, izveidota portatīva un lietotājam draudzīga magnētiskā lauka gradienta mērīšanas iekārta, kas spēj nodrošināt magnētiskā lauka mērījumus ar 500 nm telpisko izšķirtspēju.

Izmantojot pumpējoša un zondējoša lāzeru kombināciju, tika nodemonstrēts, kā ar magnetooptisko rezonanšu palīdzību tieši pētīt lāzeru inducētās fluorescences telpisko sadalījumu intensīvā lāzera starā ar Gausa jaudas sadalījuma profilu.

Abstract

This thesis is dedicated to experimental studies of dark and bright magneto-optical resonances.

By using experimental data acquired on transitions of the D_2 line of ^{85}Rb and ^{87}Rb, the conversion of bright magneto-optical resonance into dark resonances as a result of changing the laser power density of the exciting radiation at fixed laser frequency was explained for the first time.

By using experimental data acquired from an extremely thin cell and the Cs D_1 line transitions, the theoretical description of collision relaxation and fly-through relaxation was improved.

By using an extremely thin cell and the Cs D_1 line transitions, a portable and user-friendly device for magnetic field gradient measurements with 500 nm spatial resolution was constructed.

By using a combination of pump and probe lasers, a direct way to measure the fluorescence distribution in an intense laser beam with a Gaussian power distribution profile using magneto-optical resonances was demonstrated.

Andra Bērziņa promocijas darba rezultātus atspoguļojošo zinātnisko publikāciju saraksts

Zinātniskās publikācijas:

Izdevumos no LZP vispāratzīto recenzējamo zinātnisko izdevumu saraksta:

1. „Conversion of bright magneto-optical resonances into dark resonances at fixed laser frequency for D2 excitation of atomic rubidium", M. Auzinsh, A. Berzins, R. Ferber, F. Gahbauer, L. Kalvans, A. Mozers, and D. Opalevs, deviņas lapaspuses, publicēts: PHYSICAL REVIEW A 85, 033418 (2012),

2. "Relaxation mechanisms affecting magneto-optical resonances in an extremely thin cell: Experiment and theory for the cesium D1 line", M. Auzinsh, A. Berzins, R. Ferber, F. Gahbauer, U. Kalnins, L. Kalvans, R. Rundans, and D. Sarkisyan, astoņas lapaspuses, publicēts: PHYSICAL REVIEW A 91, 023410 (2015),

3. "Magnetic field gradiometer with sub-micron spatial resolution based on caesium vapour in an extremely thin cell", M. Auzinsh, A. Berzins, R. Ferber, F. Gahbauer, U. Kalnins, R. Rundans and D. Sarkisyan, astoņas lapaspuses, publicēts: LATVIAN JOURNAL OF PHYSICS AND TECHNICAL SCIENCES, N 3 (2015),

4. "Spatial dynamics of laser-induced fluorescence in an intense laser beam: experiment and theory in alkali metal atoms", M. Auzinsh, A. Berzins, R. Ferber, F. Gahbauer and U. Kalnins, astoņas lapaspuses, pieņemts publicēšanai: PHYSICAL REVIEW A.

Andra Bērziņa ieguldījuma novērtējums promocijas darba rezultātus atspoguļojošo zinātnisko publikāciju tapšanā

Zinātniskās publikācijas:

1. „Conversion of bright magneto-optical resonances into dark resonances at fixed laser frequency for D_2 excitation of atomic rubidium", M. Auzinsh, A. Berzins, R. Ferber, F. Gahbauer, L. Kalvans, A. Mozers, and D. Opalevs, deviņas lapaspuses, publicēts: PHYSICAL REVIEW A 85, 033418 (2012).
   Andra Bērziņa ieguldījums: 40% (Galvenais eksperimentālās iekārtas izveidotājs. Veikta lielākā daļa no eksperimentālajiem mērījumiem. Veikta eksperimentālo datu analīze un grafiku sagatavošana publikācijai),

2. "Relaxation mechanisms affecting magneto-optical resonances in an extremely thin cell: Experiment and theory for the cesium D_1 line", M. Auzinsh, A. Berzins, R. Ferber, F. Gahbauer, U. Kalnins, L. Kalvans, R. Rundans, and D. Sarkisyan, astoņas lapaspuses, publicēts: PHYSICAL REVIEW A 91, 023410 (2015).
   Andra Bērziņa ieguldījums: 40% (Galvenais eksperimentālās iekārtas izveidotājs. Veikta lielākā daļa no eksperimentālajiem mērījumiem un eksperimentālo datu analīze. Veikta eksperimentālās daļas apraksta izveide publikācijai),

3. "Magnetic field gradiometer with sub-micron spatial resolution based on caesium vapour in an extremely thin cell", M. Auzinsh, A. Berzins, R. Ferber, F. Gahbauer, U. Kalnins, R. Rundans and D. Sarkisyan, astoņas lapaspuses, publicēts: LATVIAN JOURNAL OF PHYSICS AND TECHNICAL SCIENCES, N 3 (2015).
   Andra Bērziņa ieguldījums: 65% (Galvenais eksperimentālās iekārtas izveidotājs. Veikta lielākā daļa no eksperimentālajiem mērījumiem un eksperimentālo datu analīze. Bijis publikācijas sagatavotājs.),

4. "Spatial dynamics of laser-induced fluorescence in an intense laser beam: experiment and theory in alkali metal atoms", M. Auzinsh, A. Berzins, R. Ferber, F. Gahbauer and U. Kalnins, deviņas lapaspuses, pieņemts publicēšanai: PHYSICAL REVIEW A (šobrīd publiski pieejams arxiv.org mājaslapā, saite: http://arxiv.org/abs/1510.07518).
   Andra Bērziņa ieguldījums: 50% (Galvenais eksperimentālās iekārtas izveidotājs. Veikta lielākā daļa no eksperimentālajiem mērījumiem un eksperimentālo datu analīze. Veikta eksperimentālās sadaļas apraksta un attēlu/grafiku izveide visai publikācijai, kā arī veikta komunikācija ar žurnāla redakciju un recenzentu, tai skaitā veikti raksta uzlabojumi (gan teksta, gan attēlu).).

Promocijas darbā izmantoto publikāciju līdzautoru piekrišana promocijas darba aizstāvēšanai uz šo publikāciju pamata

Līdzautori ar parakstu apliecina, ka piekrīt konkrētās publikācijas izmantošanai Andra Bērziņa promocijas darbā:

Publikācija:

Conversion of bright magneto-optical resonances into dark resonances at fixed laser frequency for D_2 excitation of atomic rubidium

M. Auzinsh, A. Berzins, R. Ferber, F. Gahbauer, L. Kalvans, A. Mozers, and D. Opalevs
PHYSICAL REVIEW A **85**, 033418 (2012)

Mārcis Auziņš ____________________

Ruvins Ferbers ____________________

Florian Gahbauer Florian Gahbauer

Linards Kalvāns ____________________

Artūrs Mozers ____________________

Dmitrijs Opaļevs ____________________

(LV) Promocijas darbā izmantotās publikācijas līdzautoru piekrišana promocijas darba aizstāvēšanai uz šīs publikācijas pamata

(EN) Co-authors' permission to use joint publication in the defense of the doctoral thesis based on said publication

(LV) Līdzautori ar parakstu apliecina, ka piekrīt konkrētās publikācijas izmantošanai Andra Bērziņa promocijas darbā.

(EN) With a signature co-authors permit Andris Bērziņš to use joint publication in the defense of his doctoral thesis.

(LV) Publikācija:
(EN) Publication:

Relaxation mechanisms affecting magneto-optical resonances in an extremely thin cell: Experiment and theory for the cesium D_1 line

M. Auzinsh, A. Berzins, R. Ferber, F. Gahbauer, U. Kalnins, L. Kalvans, R. Rundans and D. Sarkisyan
PHYSICAL REVIEW A **91**, 023410 (2015)

Mārcis Auziņš

Ruvins Ferbers

Florian Gahbauer Florian Gahbauer

Uldis Kalniņš

Linards Kalvāns

Ronalds Rundāns

David Sarkisyan

26.11.2015

(LV) Promocijas darbā izmantotās publikācijas līdzautoru piekrišana promocijas darba aizstāvēšanai uz šīs publikācijas pamata

(EN) Co-authors' permission to use joint publication in the defense of the doctoral thesis based on said publication

(LV) Līdzautori ar parakstu apliecina, ka piekrīt konkrētās publikācijas izmantošanai Andra Bērziņa promocijas darbā.

(EN) With a signature co-authors permit Andris Bērziņš to use joint publication in the defense of his doctoral thesis.

(LV) Publikācija:
(EN) Publication:

Magnetic field gradiometer with sub-micron spatial resolution based on caesium vapour in an extremely thin cell

M. Auzinsh, A. Berzins, R. Ferber, F. Gahbauer, U. Kalnins, R. Rundans and D. Sarkisyan
LATVIAN JOURNAL OF PHYSICS AND TECHNICAL SCIENCES, 2015, N 3

Mārcis Auziņš ____________________

Ruvins Ferbers ____________________

Florian Gahbauer Florian Gahbauer

Uldis Kalniņš ____________________

Ronalds Rundāns ____________________

David Sarkisyan ____________________

26.11.2015

Promocijas darbā izmantoto publikāciju līdzautoru piekrišana promocijas darba aizstāvēšanai uz šo publikāciju pamata

Līdzautori ar parakstu apliecina, ka piekrīt konkrētās publikācijas izmantošanai Andra Bērziņa promocijas darbā:

Publikācija:
Spatial dynamics of laser-induced fluorescence in an intense laser beam: experiment and theory in alkali metal atoms

M. Auzinsh, A. Berzins, R. Ferber, F. Gahbauer and U. Kalnins

Mārcis Auziņš ____________________

Ruvins Ferbers ____________________

Florian Gahbauer Florian Gahbauer

Uldis Kalniņš ____________________

PHYSICAL REVIEW A **85**, 033418 (2012)

Conversion of bright magneto-optical resonances into dark resonances at fixed laser frequency for D_2 excitation of atomic rubidium

M. Auzinsh,[*] A. Berzins, R. Ferber, F. Gahbauer, L. Kalvans, A. Mozers, and D. Opalevs
Laser Centre, The University of Latvia, LV-1586 Riga, Latvia

(Received 29 November 2011; published 16 March 2012)

Nonlinear magneto-optical resonances on the hyperfine transitions belonging to the D_2 line of rubidium were changed from bright to dark resonances by changing the laser power density of the single exciting laser field or by changing the vapor temperature in the cell. In one set of experiments atoms were excited by linearly polarized light from an extended cavity diode laser with polarization vector perpendicular to the light's propagation direction and magnetic field, and laser-induced fluorescence was observed along the direction of the magnetic field, which was scanned. A low-contrast bright resonance was observed at low laser power densities when the laser was tuned to the $F_g = 2 \longrightarrow F_e = 3$ transition of ^{87}Rb and near to the $F_g = 3 \longrightarrow F_e = 4$ transition of ^{85}Rb. The bright resonance became dark as the laser power density was increased above 0.6 mW/cm^2 or 0.8 mW/cm^2, respectively. When the $F_g = 2 \longrightarrow F_e = 3$ transition of ^{87}Rb was excited with circularly polarized light in a second set of experiments, a bright resonance was observed, which became dark when the temperature was increased to around 50 °C. The experimental observations at room temperature could be reproduced with good agreement by calculations based on a theoretical model, although the theoretical model was not able to describe measurements at elevated temperatures, where reabsorption was thought to play a decisive role. The model was derived from the optical Bloch equations and included all nearby hyperfine components, averaging over the Doppler profile, mixing of magnetic sublevels in the external magnetic field, and a treatment of the coherence properties of the exciting radiation field.

DOI: 10.1103/PhysRevA.85.033418 PACS number(s): 32.80.Xx, 42.50.Gy, 32.60.+i

I. INTRODUCTION

Coherences between atomic states can be exploited to modify the optical properties of a medium, which is usually an atomic vapor [1] but may also be a solid-state system [2] or an artificial atom [3]. In the phenomenon of electromagnetically induced transparency (EIT), one uses two lasers in a Λ configuration to create a coherent superposition of the two lower states that is nonabsorbing or dark [4,5]. Instead of using two laser fields and their relative detuning to create the dark coherent superposition, it is possible to create the Λ system with the two orthogonally circularly polarized components of a single, linearly polarized laser field and a ground state with degenerate magnetic sublevels. In this case, one speaks of a dark nonlinear magneto-optical resonance [6], and the coherent superposition is created or destroyed by applying a magnetic field that shifts the energies of the magnetic sublevels of a ground state with nonzero angular momentum. It is also possible to create coherent superposition states with enhanced absorption, in which case one has electromagnetically induced absorption (EIA) [7] and the related bright, nonlinear magneto-optical resonances [8] are observed. Recently, attention has been focused on the conversion of EIT to EIA as a function of the properties of the pump field, such as polarization [9] and laser power density [10–13]. In this work we investigate the conversion of a bright, nonlinear magneto-optical resonance to a dark resonance with a single laser field at fixed frequency as a function of laser power density.

A number of interesting experiments and theoretical studies have been reported recently for EIT and EIA with two light fields in the Hanle configuration. In the Hanle configuration, two atomic states are coupled in a Λ or V scheme whose legs are formed by coherent light fields of orthogonal circular polarization (see, for example, Ref. [6]). Sign changes in EIA and EIT spectra were observed on a beam of cesium atoms with copropagating pump and probe beams of various polarizations [11,14]. In this case the Doppler effect was minimal because of the atomic beam. Copropagating pump and probe beams also were used to change EIT to EIA as a function of pump intensity on the $F_g = 2 \longrightarrow F_e = 3$ transition of the D_2 line of rubidium [13]. Theoretical calculations on an analogous system of lower angular momentum were used to argue that the effect was not due to Doppler broadening but rather by population shifts caused by the two competing laser fields. However, experimental and theoretical curves could not be compared directly as the angular momentum was not the same. Similar changes from EIA to EIT were observed in the case of two counterpropagating laser fields of opposite circular polarization (Hanle configuration) from a single laser on the $F_g = 2 \longrightarrow F_e = 3$ transition of the D_2 line of ^{87}Rb [12]. Again, detailed theoretical calculations supported the conclusion that the change from EIA to EIT in the forward field were caused by the competing action of the two laser fields on the population of magnetic sublevels. However, the theoretical calculation was not done for the precise angular-momentum states studied in the experiment, and, hence, experimental and theoretical curves could not be directly compared. Interestingly, a dip in transmission was observed with linearly polarized excitation in the absence of a probe field. Our results show that changes from dips to peaks in absorption can be achieved with a single laser field in an atomic vapor, when changes in the intensity of the exciting laser radiation influence the competition between

---

[*] marcis.auzins@lu.lv

two neighboring levels and also between the polarization components of a single level. We demonstrate the ability of computational models to describe these effects in detail by directly comparing experimental and theoretical curves.

Dark, nonlinear magneto-optical resonances have been known for a long time [15] and studied in great detail. Bright resonances attracted attention [8] and were explained [16,17] more recently. For linearly polarized exciting radiation, bright resonances can appear when the total angular momentum of the excited state F_e is greater than the total angular momentum of the ground state F_g. Unlike dark resonances, in which a coherent dark state is formed, bright resonances occur when atomic populations are redistributed by various excitation and relaxation cycles into states that interact more strongly with the exciting radiation. Thus, bright resonance contrast on open transitions, if observable at all, is very small. Observing bright resonances is complicated by the fact that in most alkali-metal systems, the excited state hyperfine structure (HFS) is only partially resolved under Doppler broadening. Thus, even when the laser is tuned to a bright resonance, neighboring dark resonances can be excited in atoms belonging to different velocity groups. The extent to which neighboring transitions are excited can also depend on power broadening of the laser. A further complication arises from the fact that some hyperfine transitions are cycling, while others are partially open. In the case of cycling transitions, atoms are redistributed among different coherent atomic states of the same hyperfine level according to the respective transitions strengths. In partially open transitions, population can be lost to other hyperfine levels. In any case, the intensity of the exciting laser must be taken into account. As a result, in order to make realistic comparisons between experiment and theory, it is important to have a good model that takes into account the finite laser linewidth, Doppler broadening and power broadening, and the nonlinear Zeeman splitting with the mixing of magnetic sublevels in the magnetic field.

In the experimental conditions studied here, the problem is highly nonlinear and it is not possible to give a complete description with analytical models. Numerical models based on the optical Bloch equations were developed, first, for atomic beams [18], in which Doppler broadening is minimal. In time, such models were expanded to include Doppler broadening and neighboring hyperfine transitions [19], but a detailed treatment of the coherence properties of the laser radiation was not included. When the coherence properties of the laser radiation were included [20,21], along with averaging over the Doppler profile, good agreement between theoretical and experimental signals for nonlinear magneto-optical resonances could be achieved, for example, for D_1 excitation in cesium [22] and rubidium [23]. D_2 excitation in rubidium presents an additional challenge, because the hyperfine splitting of the excited state is smaller relative to the Doppler broadening than in the case of D_1, and so neighboring states influence more strongly.

In this work, we report that when a single, linearly polarized laser field was tuned to the $F_g = 2 \longrightarrow F_e = 3$ transition of ^{87}Rb and the $F_g = 3 \longrightarrow F_e = 4$ transition of ^{85}Rb, bright resonances became dark when the laser power density was increased. Experimental measurements were reproduced by theoretical calculations conducted for the same transition that was measured. The sensitivity of the resonances' shapes to the experimental parameters provided a stringent test of the theoretical model. As an additional example of a resonance that changes sign for fixed laser frequency and as stimulus for further study, we also present measurements of a fluorescence maximum that becomes a minimum as the temperature is increased for circularly polarized excitation of the $F_g = 2 \longrightarrow F_e = 3$ transition of ^{87}Rb.

II. EXPERIMENTAL DESCRIPTION

Figure 1 shows the level scheme of the D_2 line of rubidium. Note that the hyperfine transitions of the excited state of the ^{85}Rb D_2 line are essentially unresolved under the typical Doppler broadening at room temperature, which has a full width at half maximum (FWHM) of approximately 500 MHz, while they are partially resolved in the case of ^{87}Rb.

The geometry of the excitation in the experiment is given in Fig. 2. The exciting laser radiation was linearly polarized with polarization vector perpendicular to the magnetic field and to the propagation direction of the radiation. For some experiments, a Thorlabs achromatic $\lambda/4$ plate was inserted after the linear polarizer to produce circularly polarized radiation in the cell. The observation direction was parallel to the magnetic field.

The laser was an external cavity diode laser. The temperature of the box and the diode were stabilized by Thorlabs TED200 temperature controllers, and the current was controlled by a Thorlabs LDC205B current controller. The laser frequency was stabilized manually, and the frequency drift during a typical data-taking run was typically around 10 MHz or less. The wavelength was monitored by a HighFinesse WS-7 wavemeter. A Thorlabs BP104-VIS beam profiler was used to measure the beam diameter, which was taken to be the FWHM of the intensity distribution. The cell was a 25-mm-long pyrex cell with optical quality windows filled with natural rubidium and produced by Toptica, A.G. The laser radiation entered the cell through a Glan-Thompson polarizer. A combination

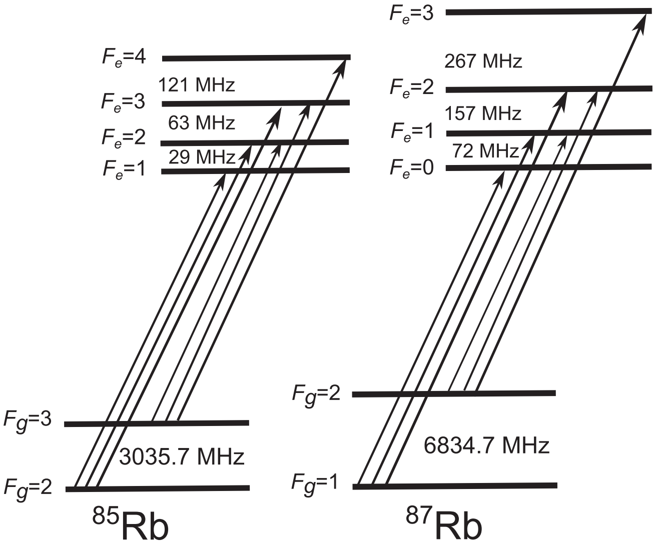

FIG. 1. Hyperfine level structure and transitions of the D_2 line of rubidium.

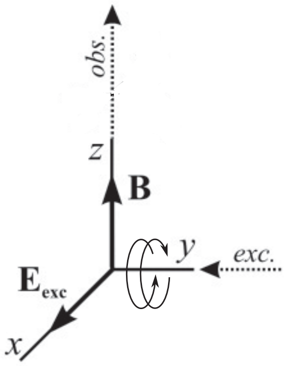

FIG. 2. Experimental geometry. The relative orientation of the laser beam (*exc*), laser light polarization ($\mathbf{E}_{\text{exc}}$), magnetic field ($\mathbf{B}$), and observation direction (*obs*). Circularly polarized light could be produced by means of a $\lambda/4$ plate.

of neutral density filters and a polarization rotator before the polarizer was used to select various laser power densities. The laser-induced fluorescence (LIF) was focused onto a Thorlabs FDS100 photodiode and amplified. Signals were recorded by an Agilent DSO5014A oscilloscope.

The cell was located at the center of a three-axis Helmholtz coil. Two coils were used to compensate the ambient magnetic field. The residual magnetic field was estimated to be less than 10 mG. The third coil was used to scan the magnetic field along the z axis as indicated in Fig. 2 using a bipolar BOP-50-8-M power supply from Kepco. In order to find the appropriate current for the field compensation, the polarization vector of the laser beam was rotated parallel to the z axis and the magnetic field was scanned along the z axis while the current in the compensating coils was adjusted in order to eliminate the magneto-optical resonance that appears when the field is not compensated. The cell was at room temperature, except for those experiments that investigated the temperature dependence, when the cell was heated with hot air. The air was heated some distance away from the cell to avoid stray magnetic fields from the heating currents. The temperature was measured with two thermocouples near the cell, though the thermocouples were removed during the measurements as they were slightly magnetized.

III. THEORETICAL MODEL

The atomic state was described by a density matrix ρ in the ξ,F,m_F basis, where F denotes the total atomic angular-momentum quantum number (that characterizes the hyperfine structure), m_F labels the respective magnetic quantum number for Zeeman splitting, and ξ represents all other quantum numbers. The fluorescence signal can be calculated from the part of the density matrix that describes the population and Zeeman coherences of the excited state $\rho_{e_ie_j}$. To do so, the optical Bloch equations (OBEs) that describe the time evolution of a density matrix were employed [24]:

$$i\hbar\frac{\partial\rho}{\partial t} = [\hat{H},\rho] + i\hbar\hat{R}\rho. \tag{1}$$

We assumed that the interaction between the atoms and the exciting field was described in the dipole approximation by the interaction operator $\hat{V} = -\hat{\mathbf{d}}\cdot\mathbf{E}(t)$. The electric field $\mathbf{E}(t)$ was treated as a classically oscillating field with a stochastically fluctuating phase. As the energy shifts due to the magnetic field were small compared to the fine-structure splitting, the Hamiltonian of the atomic interaction with the magnetic field could be written as

$$\hat{H}_B = \frac{\mu_B}{\hbar}(g_J\mathbf{J} + g_I\mathbf{I})\cdot\mathbf{B}, \tag{2}$$

and expanded as shown, for example, in Ref. [25]. We denote the unperturbed atomic Hamiltonian as $\hat{H}_0$, and so the full Hamiltonian of the system is

$$\hat{H} = \hat{H}_0 + \hat{H}_B + \hat{V}. \tag{3}$$

The relaxation operator $\hat{R}$ in Eq. (1) consists of the spontaneous emission rate, equal to the natural linewidth Γ of the transition and the transit relaxation rate γ, which comes about because the moving atoms spend a finite time in the laser beam. The rate of atom-atom collisions in our experimental conditions (vacuum cell at room temperature) were estimated to be at least two orders of magnitude less than the transit relaxation rate and, therefore, were neglected.

The OBEs [Eq. (1)] were treated to obtain rate equations for the Zeeman coherences of the ground and excited states. The treatment included the rotating-wave approximation [26], averaging and decorrelation of the stochastic phase [27], and adiabatic elimination of the optical coherences (see Ref. [21] for details). As a result, the following rate equations were obtained:

$$\begin{aligned}\frac{\partial\rho_{g_ig_j}}{\partial t} &= \left(\Xi_{g_ie_m} + \Xi^*_{e_kg_j}\right)\sum_{e_k,e_m} d^*_{g_ie_k}d_{e_mg_j}\rho_{e_ke_m}\\ &\quad - \sum_{e_k,g_m}\left(\Xi^*_{e_kg_j}d^*_{g_ie_k}d_{e_kg_m}\rho_{g_mg_j} + \Xi_{g_ie_k}d^*_{g_me_k}d_{e_kg_j}\rho_{g_ig_m}\right)\\ &\quad - i\omega_{g_ig_j}\rho_{g_ig_j} - \gamma\rho_{g_ig_j} + \sum_{e_ke_l}\Gamma^{e_ke_l}_{g_ig_j}\rho_{e_ke_l} + \lambda\delta(g_i,g_j)\end{aligned} \tag{4a}$$

$$\begin{aligned}\frac{\partial\rho_{e_ie_j}}{\partial t} &= \left(\Xi^*_{e_ig_m} + \Xi_{g_ke_j}\right)\sum_{g_k,g_m} d_{e_ig_k}d^*_{g_me_j}\rho_{g_kg_m}\\ &\quad - \sum_{g_k,e_m}\left(\Xi_{g_ke_j}d_{e_ig_k}d^*_{g_ke_m}\rho_{e_me_j} + \Xi^*_{e_ig_k}d_{e_mg_k}d^*_{g_ke_j}\rho_{e_ie_m}\right)\\ &\quad - i\omega_{e_ie_j}\rho_{e_ie_j} - (\Gamma+\gamma)\rho_{e_ie_j}.\end{aligned} \tag{4b}$$

In Eq. (4) the Zeeman coherences of the ground and excited states are denoted by $\rho_{g_ig_j}$ and $\rho_{e_ie_j}$, respectively. Each term of the rate equations describes a well-defined part of the atom-light interaction process. Thus, the first terms in both Eqs. (4a) and (4b) describe the population increase and the creation of Zeeman coherences, and the second terms denote the population decrease and the destruction of Zeeman coherences in the respective atomic state (ground or excited) due to the laser-induced transitions; $d_{e_ig_j}$ is the dipole transition matrix element between the ground state i and the excited state j [28], while $\Xi_{e_ig_j}$ describes the rate of the atomic transitions induced by the exciting radiation and is defined below [Eq. (5)]. The third term of Eqs. (4) describes the destruction of the Zeeman coherences by the external magnetic field; ω_{ij} is the splitting of the Zeeman sublevels. The fourth term describes the relaxation processes, and the fifth and sixth [absent in Eq. (4b)] describe the repopulation of the ground state due to spontaneous transitions and "fresh" atoms flying into the region of the interaction. It was assumed that the atomic equilibrium density outside the interaction region is normalized to unity, and so $\lambda = \gamma$. The transit relaxation rate was used as an adjustable parameter and corresponds to the average time spent by the atoms in the interaction region.

The interaction strength $\Xi_{e_i g_j}$ is given by

$$\Xi_{e_i g_j} = \frac{|\varepsilon_{\bar{\omega}}|^2}{\hbar^2} \frac{1}{\frac{\Gamma+\gamma+\Delta\omega}{2} + i(\bar{\omega} - \mathbf{k}_{\bar{\omega}} \cdot \mathbf{v} - \omega_{e_i g_j})}, \qquad (5)$$

where $\Delta\omega$ is the linewidth of the exciting radiation of central frequency $\bar{\omega}$ and $\mathbf{k}_{\bar{\omega}} \cdot \mathbf{v}$ is the frequency shift due to the Doppler effect. The value $\frac{|\varepsilon_{\bar{\omega}}|}{\hbar}$ is proportional to the Rabi frequency, which describes the coupling strength induced by the oscillating electric field between the chosen atomic states as follows:

$$\Omega_R^2 = \frac{|\varepsilon_{\bar{\omega}}|^2}{\hbar^2} \|d\|^2, \qquad (6)$$

where $\|d\|$ is the reduced dipole transition matrix element, which is equal for all d_{ij} elements in Eqs. (4). The Rabi frequency squared is proportional to the exciting radiation's power density with some proportionality coefficient k_{Rabi},

$$I = k_{\text{Rabi}} \Omega_R^2, \qquad (7)$$

and it is used as an adjustable parameter that corresponds to the exciting radiation's power density.

The experiments took place under stationary excitation conditions, for which Eqs. (4) are valid. Thus, $\frac{\partial \rho_{g_i g_j}}{\partial t} = \frac{\partial \rho_{e_i e_j}}{\partial t} = 0$, and the differential equations [Eqs. (4)] were reduced to a system of linear equations that could be solved to obtain the density matrix components that describe the Zeeman coherences of both the atomic ground and excited states. From the obtained density matrix, the fluorescence signal was calculated as

$$I_{fl}(\vec{e}) = \tilde{I}_0 \sum_{g_i, e_j, e_k} d_{g_i e_j}^{(ob)*} d_{e_k g_i}^{(ob)} \rho_{e_j e_k}, \qquad (8)$$

where $\tilde{I}_0$ is a constant of proportionality and $d_{ij}^{(ob)}$ is the matrix element of the dipole transition at the observation geometry.

A summation over the different atomic velocity groups, associated to different $\mathbf{v}$ in Eq. (5), was performed to describe the Doppler broadening of the transitions. When the density matrix and the fluorescence signal were calculated, we took into account all nearby hyperfine transitions of both the ground and the excited states, represented by different $w_{e_i g_j}$ in Eq. (5). Atomic constants were taken from Refs. [25,29]. Some parameters could not be determined directly with certainty. Starting from reasonable estimates, these parameter values were varied in different sets of simulations in order to find the set of parameters that provided the best overall agreement between experiment and theory. We required the parameter values to be consistent for all measurements, even if the agreement between theory and experiment for individual cases was not the best that could have been achieved by tailoring the parameters for each case. Thus, the laser linewidth was assumed to be $\Delta\omega = 2$ MHz. The proportionality constant k_{Rabi} between the laser power density I and the square of the Rabi frequency Ω ($I = k_{\text{Rabi}} \Omega^2$) was $k_{\text{Rabi}} = 0.575$, with the Rabi frequency given in MHz and the laser power density in mW/cm^2. The relationship between the transit relaxation rate γ and the laser beam diameter d was $\gamma = 0.0033/d$ with the transit relaxation rate in MHz and the laser beam diameter in cm. The standard deviation of the Doppler profile was assumed to be 216 MHz, and it was sampled with a step size of less than 2 MHz during the averaging over the Doppler distribution. No additional background was subtracted beyond the background determined during the experiment by blocking the laser beam.

IV. RESULTS AND DISCUSSION

The fluorescence signals recorded as a function of magnetic field usually showed two kinds of structure. One structure was broad, with a width on the order of several gauss. This structure was caused by coherences in the excited state as well as by Zeeman sublevels being shifted out of resonance with the laser. The broad structure also tended to have a strong contrast, on the order of several percent or even tens of percent. In addition to the broad structure, it was also possible to observe narrow features, centered around zero magnetic field, with widths on the order of several hundred milligauss. These resonances were related to the destruction of coherences in the ground state as a magnetic field breaks the degeneracy of the magnetic sublevels. The features were also very small, with contrasts from a fraction of a percent to a few percent. (We defined the contrast of the narrow structure with respect to the estimated zero-field value of the curve corresponding to the larger structure.) Our study was focused on these narrow resonances and the way their contrast and even their sign depended on the laser power density and temperature. Thus, in the results that follow, only a narrow range of the magnetic field is shown.

Figure 3 shows the LIF intensity as a function of magnetic field for various values of the power density of the exciting laser radiation with the laser tuned to the $F_g = 2 \longrightarrow F_e = 3$ transition of ^{87}Rb. The laser beam diameter was 2.1 mm. This transition could be expected to be bright because $F_g < F_e$. Indeed, a very weak bright resonance with contrast on the order of 0.3% was observed when the laser power density was 0.14 mW/cm^2. However, as the power density of the exciting laser radiation was increased, the bright resonance disappeared and became dark for laser power densities greater than about 0.6 mW/cm^2. At a laser power density of 2.9 mW/cm^2, the contrast of the dark resonance with respect to the intensity at the inflection point of the larger structure was about 2%. The resonances appeared to be somewhat narrower in the calculations than in the experiment. The reason for this discrepancy was most likely a residual transverse magnetic field on the order of a few milligauss. It should also be pointed out that the model made the simplifying assumption that the laser power density was constant over the laser beam width, whereas in reality there was a distribution of laser power densities. Nevertheless, given the subtle nature of the effect, the agreement between experiment and theory was acceptable.

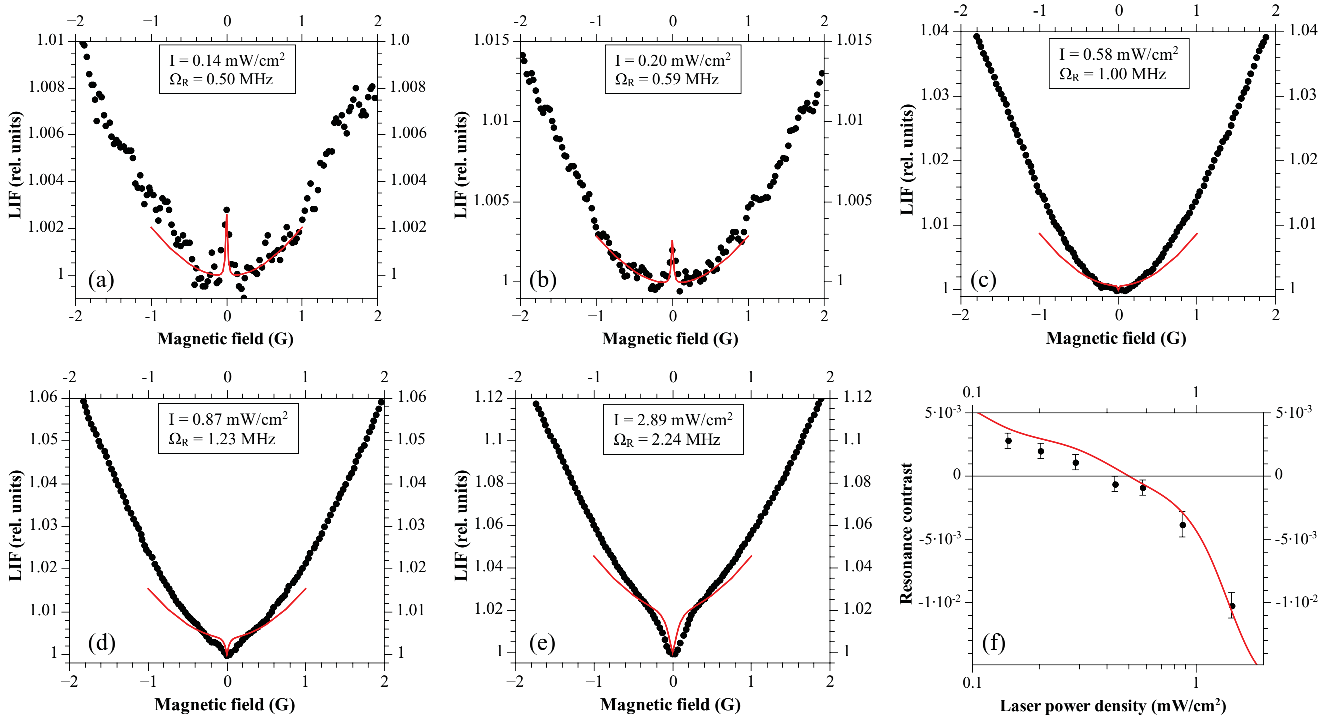

FIG. 3. (Color online) Bright and dark resonances for various laser-power densities with the laser tuned to the $F_g = 2 \longrightarrow F_e = 3$ transition of ^{87}Rb for linearly polarized exciting laser radiation with a beam diameter of 2.1 mm. Markers represent the experimental results, whereas the solid line represents the results of calculations. The final panel shows the contrast of the narrow resonance referenced to the estimated background due to the broad structure at zero magnetic field.

The theoretical model unambiguously reproduced the change from a bright to a dark resonance for laser power densities above $I = 0.4$ mW/cm^2. In order to understand the effect qualitatively, one must keep in mind that Doppler broadening allows the laser to excite the neighboring $F_g = 2 \longrightarrow F_e = 2$ transition, and so the observed signal is the result of a superposition of the bright resonance at the $F_g = 2 \longrightarrow F_e = 3$ transition and the dark resonance at the $F_g = 2 \longrightarrow F_e = 2$ transition. Figure 4 shows the calculated contrasts as a function of laser power density for laser radiation in resonance with each of these two transitions

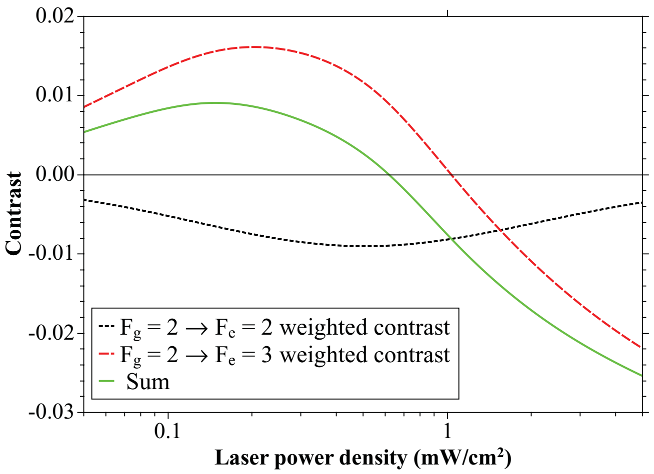

FIG. 4. (Color online) Calculated contrasts as a function of laser power density of the resonances at the $F_g = 2 \longrightarrow F_e = 2$ and $F_g = 2 \longrightarrow F_e = 3$ transitions of ^{87}Rb weighted by the relative number of atoms in the velocity group that is in resonance with a laser tuned to the $F_g = 2 \longrightarrow F_e = 3$ transition.

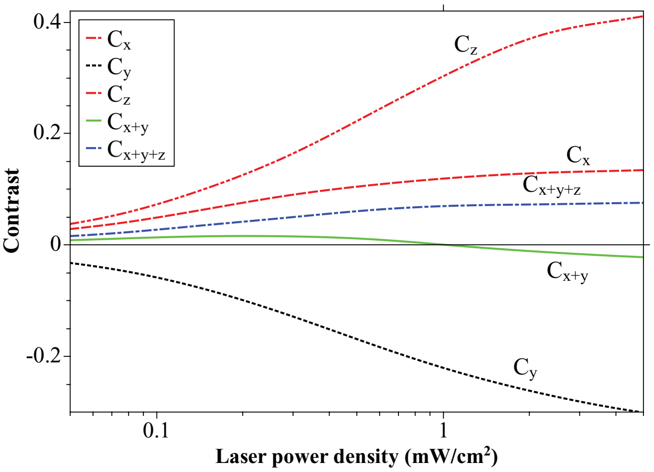

FIG. 5. (Color online) Contrast as a function of laser power density of the resonance at the $F_g = 2 \longrightarrow F_e = 3$ transition of ^{87}Rb when particular polarization components of the fluorescence intensity I are observed. The curves give the contrasts C_x, C_y, C_z, C_{x+y}, and C_{x+y+z} for the three orthogonal polarization components of the fluorescence I_x, I_y, and I_z, as well as for the components I_{x+y} and I_{x+y+z}. The calculations were performed without taking into account the Doppler effect. Note that the contrast is a relative figure, whereas the intensities I_x, I_y, and I_z differ in their dependence on laser power density and magnetic field. Note also that the solid green line represents the same quantity as the solid green line in Fig. 4.

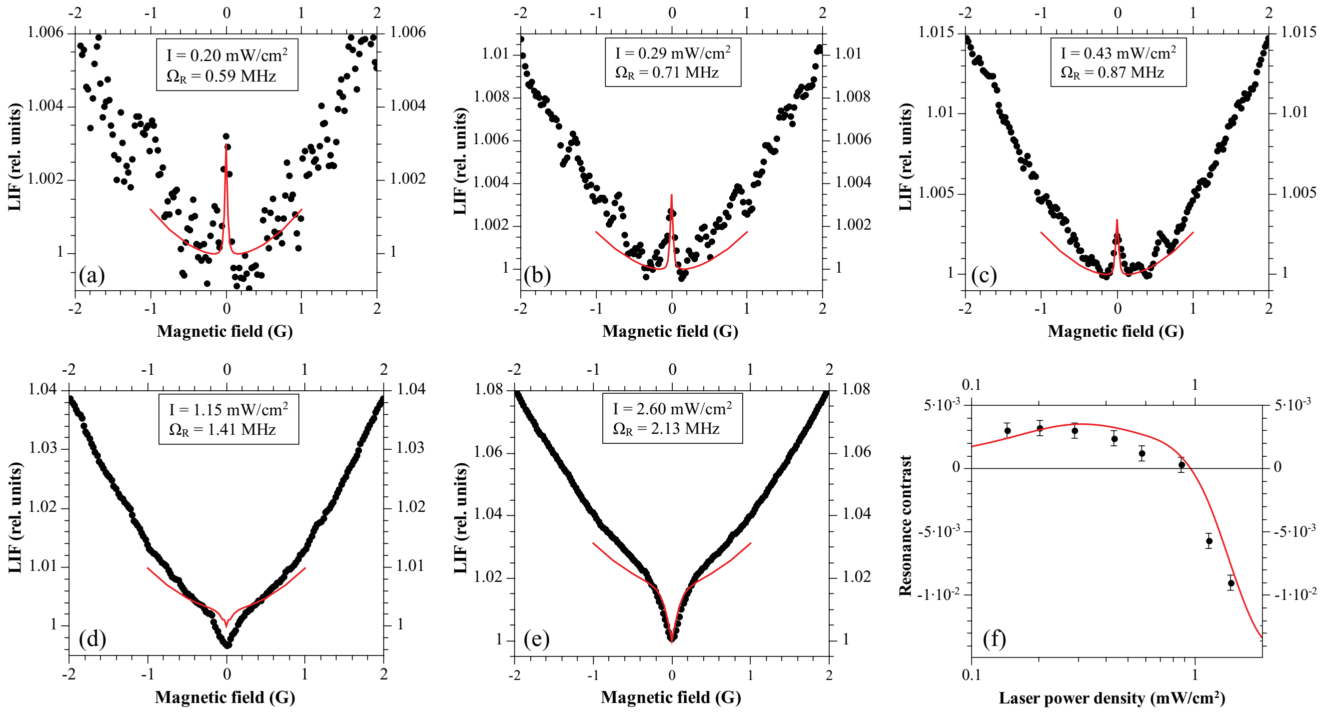

FIG. 6. (Color online) Bright and dark resonances obtained at various laser power densities near the $F_g = 3 \longrightarrow F_e = 4$ transition of ^{85}Rb. The laser was detuned from the exact transition by 200 MHz in the direction away from the $F_g = 3 \longrightarrow F_e = 4$ transition for linearly polarized exciting laser radiation with a beam diameter of 2.1 mm. Markers represent the experimental results, whereas the solid line represents the results of calculations. The final panel shows the contrast of the narrow resonance referenced to the estimated background due to the broad structure at zero magnetic field.

but ignoring Doppler broadening. The curves in that figure suggest that the bright resonance at the $F_g = 2 \longrightarrow F_e = 3$ transition would become dark in any case for laser power densities above a few mW/cm^2, even without the influence of the neighboring transition. There is no reason why a bright resonance should become dark merely because of a change in laser-power density. However, while a resonance that includes the total fluorescence must remain bright, different polarization components of this fluorescence may behave differently, and in the experiment not all polarization components were observed. Figure 5 shows the calculated contrast of resonances observed for each of three orthogonally polarized fluorescence components: the x and z components

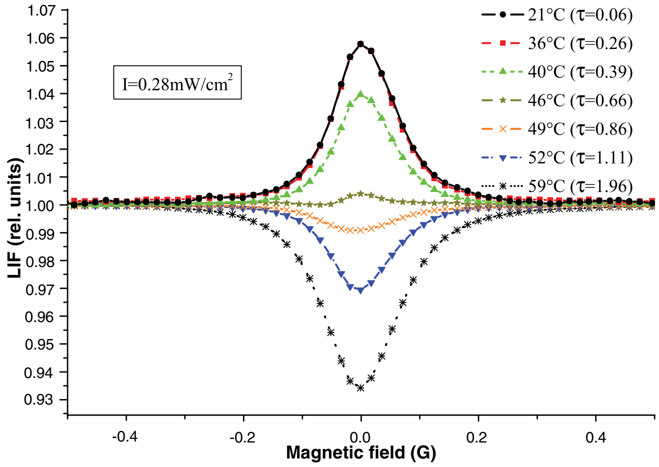

FIG. 7. (Color online) Dark and bright resonances obtained at various vapor temperatures at the $F_g = 2 \longrightarrow F_e = 3$ transition of ^{87}Rb for circularly polarized excitation at a laser-power density of around 0.28 mW/cm^2. Experimental measurements are shown. The optical depth τ along the laser beam inside the cell is given in parentheses next to the temperature. The curves for 21 °C and 36 °C overlap.

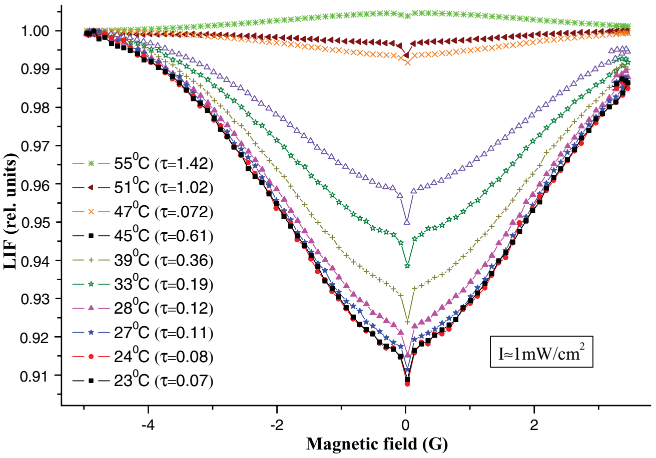

FIG. 8. (Color online) Dark resonances obtained at various vapor temperatures at the $F_g = 2 \longrightarrow F_e = 3$ transition of ^{87}Rb for linearly polarized excitation at a laser power density of around 1 mW/cm^2. Experimental measurements are shown. The optical depth τ along the laser beam inside the cell is given in parentheses next to the temperature.

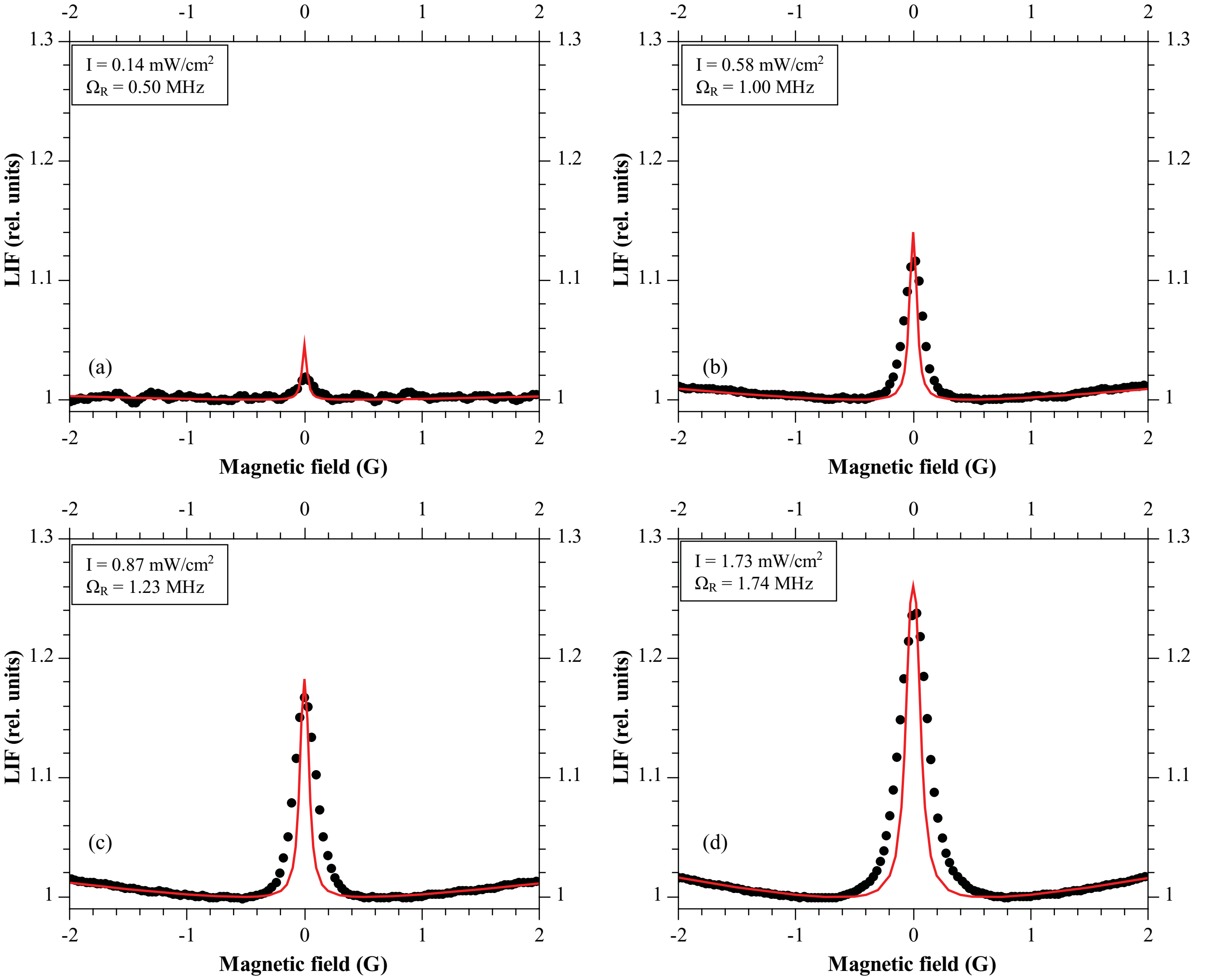

FIG. 9. (Color online) Bright resonances obtained at various laser power densities for circularly polarized excitation of the $F_g = 2 \longrightarrow F_e = 3$ transition of ^{87}Rb. Markers represent the experimental results, whereas the solid line represents the results of calculations.

always give a bright resonance, while the y component is always dark. In our observation geometry we registered the x and y components, and, as can be seen in the figure, the contrast of the "dark" y component changes more rapidly. When the contrasts are weighted by the actual fluorescence intensities, the y component actually becomes dominant at larger excitation power densities. Nevertheless, in the total fluorescence emitted in all directions (labelled C_{x+y+z} in Fig. 5) a bright resonance still would be observed. In other words, at each value of the magnetic field, the degree of polarization is a function of laser power density, and, in a particular observation geometry, this dependence can change the contrast of a resonance from bright to dark.

Figure 6 shows magneto-optical resonances obtained near the $F_g = 3 \longrightarrow F_e = 4$ transition of ^{85}Rb but with the laser detuned by 200 MHz in the direction away from the $F_g = 3 \longrightarrow F_e = 3$ transition. A bright resonance was observed at very low laser power densities. Similarly to the case of the $F_g = 2 \longrightarrow F_e = 3$ transition of ^{87}Rb, the resonance became dark for laser power densities greater than 0.8 mW/cm^2. When the laser was tuned directly to the $F_g = 3 \longrightarrow F_e = 4$ transition of ^{85}Rb, no bright resonance was observed even for laser power densities as low as 0.14 mW/cm^2. The reason was probably the influence of the strong dark resonance at the nearby $F_g = 3 \longrightarrow F_e = 3$ transition, which could be excited for some velocity groups of atoms. Power broadening may also have played a small role in exciting this nearby transition. Even if the $F_g = 3 \longrightarrow F_e = 3$ transition was excited only weakly, it could easily overwhelm the bright resonance at the $F_g = 3 \longrightarrow F_e = 4$ transition. The laser beam diameter for this series of measurements was 2.1 mm.

Figure 7 shows the fluorescence signals obtained at the $F_g = 2 \longrightarrow F_e = 3$ transition of ^{87}Rb at various vapor temperatures and for circularly polarized excitation. The elevated temperatures were achieved by conducting hot air around the cell as described in Sec. II. As the temperature was increased, the contrast of the bright resonance decreased until the bright resonance disappeared at around 40 °C. At this temperature, the optical depth traversed by the laser beam in the 25-mm-long cell was ~0.39. At higher temperatures, a dark resonance was observed, and its contrast grew with increasing temperature. The change from bright to dark resonance around an optical depth of 0.66 was probably related to reabsorption. With each reabsorption cycle, information about the original coherent atomic state is lost. This hypothesis is supported by the fact that the optical depth at which the bright resonance disappeared ($\sim$0.66) roughly corresponded to the optical depth at which the ratio of the incoherent pumping rate to other relaxation rates reaches 1.5 and continues to increase (see Ref. [30], Fig. 5). Similar measurements were made for linearly polarized light (see Fig. 8). In that case, although the contrast of the dark resonance decreased with temperature, it never changed sign. The case of circularly polarized light had been studied earlier in the context of CPT resonances, and a similar change in resonance sign with temperature had been observed [31].

Our theoretical model did not include effects that become important at elevated temperatures, such as reabsorption. Thus, the change from bright to dark of the resonance at the $F_g = 2 \longrightarrow F_e = 3$ transition of ^{87}Rb excited by circularly polarized light could not be reproduced by our model. Nevertheless, the model could be checked against the results at room temperature.

Figure 9 shows measured and calculated signals for bright resonances obtained by exciting the $F_g = 2 \longrightarrow F_e = 3$ transition of ^{87}Rb with circularly polarized laser radiation at various laser power densities. The rubidium vapor was at room temperature. The change in temperature was accompanied by a change from bright to dark resonance with contrasts on the order of 6%, much larger than in the case of linearly polarized excitation. The theoretical calculations showed somewhat narrower resonances than the experiment. However, the large contrast was described well, and even the agreement between experiment and theory for the broad structure was better than in the case of the small bright resonances observed under linear excitation. Again, the model's idealization of the laser beam profile should be kept in mind.

V. CONCLUSION

Nonlinear magneto-optical resonances in the hyperfine transitions of the D_2 line of atomic rubidium have been studied under excitation by a single laser field. When the exciting laser radiation was linearly polarized, bright resonances were observed at the $F_g = 2 \longrightarrow F_e = 3$ transition of ^{87}Rb and at the $F_g = 3 \longrightarrow F_e = 4$ transition of ^{85}Rb when the laser power density was very low. However, as the laser power density was increased above 0.6 mW/cm^2 or 0.8 mW/cm^2, respectively, these bright resonances became dark. The effect was described by a theoretical model based on the optical Bloch equations, which took into account all nearby hyperfine transitions, the mixing of magnetic sublevels in the external magnetic field, the coherence properties of the laser radiation, and the Doppler broadening. The parameter values in the model that could not be measured precisely were adjusted once for the entire set of measurements. These parameters were the coefficient that relates transit relaxation rate to the laser beam diameter, the coefficient that relates laser power density to the squared Rabi frequency, and the laser linewidth. The possibility of examining the density matrix calculated for the precise system under study provided useful insight into the role of competing effects that take place in the experiment.

In the case of circularly polarized excitation of the $F_g = 2 \longrightarrow F_e = 3$ transition of ^{87}Rb, a bright resonance was observed at room temperature, but this bright resonance became dark as the vapor temperature was increased. The change might be related to reabsorption effects.

The ability of the model to describe subtle effects, such as the change from bright to dark resonances in a system whose hyperfine structure was not resolved under Doppler broadening confirmed that the model is an adequate tool for studying nonlinear magneto-optical resonances in spite of its simplifying assumptions about the transit relaxation time and the laser power density distribution. In order to test its utility in understanding other systems, the model was applied retrospectively to previously published results in which a simpler theory failed to describe the measured results. In that case (see Ref. [32], Fig. 3a), a broad dark resonance was measured at low power on the the $F_g = 3 \longrightarrow F_e = 3,4,5$ transition of cesium excited with linearly polarized light, but the theory, which included only the cycling transition, predicted a narrow bright resonance. Our model was able to show the correct sign and width of the resonance, which underlines the need for detailed theoretical treatments. Work is currently in progress to apply the model to describing nonzero resonance signals (see, for example, Ref. [33]) and nonlinear magneto-optical resonances for D_2 excitation in a rubidium vapor cell with a width of several hundred nanometers (see, for example, Ref. [34]). However, the ability to change a bright resonance into a dark resonance by increasing the temperature suggests that, in the future, reabsorption effects should be included in the model.

ACKNOWLEDGMENTS

We thank Andrey Jarmola for helpful advice and discussions. We gratefully acknowledge support from the Latvian State Research Programme Grant No. 2010/10-4/VPP-2/1, ERAF project no. 2DP/2.1.1.1.0/10/APIA/VIAA/036, and ESF project no. 2009/0223/1DP/1.1.1.2.0./09/APIA/VIAA/008.

[1] E. Arimondo, in *Progress in Optics*, edited by E. Wolf, Vol. 35 (Elsevier, Amsterdam, 1996), pp. 257–354 [http://www.sciencedirect.com/science/article/pii/S0079663808705316].

[2] P. R. Hemmer, A. V. Turukhin, M. S. Shahriar, and J. A. Musser, Opt. Lett. **26**, 361 (2001).

[3] W. R. Kelly, Z. Dutton, J. Schlafer, B. Mookerji, T. A. Ohki, J. S. Kline, and D. P. Pappas, Phys. Rev. Lett. **104**, 163601 (2010).

[4] S. E. Harris, J. E. Field, and A. Imamoglu, Phys. Rev. Lett. **64**, 1107 (1990).

[5] M. Fleischhauer, A. Imamoglu, and J. P. Marangos, Rev. Mod. Phys. **77**, 633 (2005).

[6] D. Budker, W. Gawlik, D. F. Kimball, S. M. Rochester, V. V. Yashchuk, and A. Weis, Rev. Mod. Phys. **74**, 1153 (2002).

[7] A. M. Akulshin, S. Barreiro, and A. Lezama, Phys. Rev. A **57**, 2996 (1998).

[8] Y. Dancheva, G. Alzetta, S. Cartalava, M. Taslakov, and C. Andreeva, Opt. Commun. **178**, 103 (2000).

[9] D. V. Brazhnikov, A. V. Taichenachev, A. M. Tumaikin, V. I. Yudin, I. I. Ryabtsev, and V. M. Entin, JETP Lett. **91**, 625 (2010).

[10] H. H. Kim, M. H. Ahn, K. Kim, J. B. Kim, and H. S. Moon, J. Korean Phys. Soc. **46**, 1109 (2005).

[11] K. Dahl, L. S. Molella, R.-H. Rinkleff, and K. Danzmann, Opt. Lett. **33**, 983 (2008).

[12] A. A. Zhukov, S. A. Zibrov, G. V. Romanov, Y. O. Dudin, V. V. Vassiliev, V. L. Velichansky, and V. P. Yakovlev, Phys. Rev. A **80**, 033830 (2009).

[13] N. Ram and M. Pattabiraman, J. Phys. B **43**, 245503 (2010).

[14] L. S. Molella, K. Dahl, R.-H. Rinkleff, and K. Danzmann, Opt. Commun. **282**, 3481 (2009).

[15] J. C. Lehmann and C. Cohen-Tannoudji, C. R. Acad. Sci. (Paris) **258**, 4463 (1964).

[16] F. Renzoni, S. Cartaleva, G. Alzetta, and E. Arimondo, Phys. Rev. A **63**, 065401 (2001).

[17] J. Alnis and M. Auzinsh, Phys. Rev. A **63**, 023407 (2001).

[18] J. L. Picqué, J. Phys. B **11**, L59 (1978).

[19] C. Andreeva, S. Cartaleva, Y. Dancheva, V. Biancalana, A. Burchianti, C. Marinelli, E. Mariotti, L. Moi, and K. Nasyrov, Phys. Rev. A **66**, 012502 (2002).

[20] Y. P. Malakyan, S. M. Rochester, D. Budker, D. F. Kimball, and V. V. Yashchuk, Phys. Rev. A **69**, 013817 (2004).

[21] K. Blushs and M. Auzinsh, Phys. Rev. A **69**, 063806 (2004).

[22] M. Auzinsh, R. Ferber, F. Gahbauer, A. Jarmola, and L. Kalvans, Phys. Rev. A **78**, 013417 (2008).

[23] M. Auzinsh, R. Ferber, F. Gahbauer, A. Jarmola, and L. Kalvans, Phys. Rev. A **79**, 053404 (2009).

[24] S. Stenholm, *Foundations of Laser Spectroscopy* (Dover, Mineoloa, NY, 2005).

[25] D. A. Steck, *Rubidium 85 d line data* (Sep. 2009; revision 2.1.2, 12 August 2009) [http://steck.us/alkalidata].

[26] L. Allen and J. H. Eberly, *Optical Resonance and Two Level Atoms* (Wiley, New York, 1975).

[27] N. G. van Kampen, Phys. Rep. **24**, 171 (1976).

[28] M. Auzinsh, D. Budker, and S. M. Rochester, Phys. Rev. A **80**, 053406 (2009).

[29] D. A. Steck, *Rubidium 87 d line data* (Aug. 2009; revision 2.1.2, 12 August 2009) [http://steck.us/alkalidata].

[30] A. B. Matsko, I. Novikova, and G. R. Welch, J. Mod. Opt. **49**, 367 (2002).

[31] S. Gozzini, L. Marmugi, D. Slavov, A. Lucchesini, and S. Cartaleva, Proc. SPIE **7747**, 77470O (2011).

[32] A. V. Papoyan, M. Auzinsh, and K. Bergmann, Eur. Phys. J. D **21**, 63 (2002).

[33] J. Alnis, K. Blushs, M. Auzinsh, S. Kennedy, N. Shafer-Ray, and E. Abraham, J. Phys. B **36**, 1161 (2003).

[34] M. Auzinsh, R. Ferber, F. Gahbauer, A. Jarmola, L. Kalvans, A. Papoyan, and D. Sarkisyan, Phys. Rev. A **81**, 033408 (2010).

PHYSICAL REVIEW A **91**, 023410 (2015)

Relaxation mechanisms affecting magneto-optical resonances in an extremely thin cell: Experiment and theory for the cesium D_1 line

M. Auzinsh,[1,*] A. Berzins,[1] R. Ferber,[1] F. Gahbauer,[1] U. Kalnins,[1] L. Kalvans,[1] R. Rundans,[1] and D. Sarkisyan[2]
[1]*Laser Centre, The University of Latvia, 19 Rainis Boulevard, LV-1586 Riga, Latvia*
[2]*Institute for Physical Research, NAS of Armenia, Ashtarak-0203, Armenia*

(Received 12 November 2014; published 10 February 2015)

We have measured magneto-optical signals obtained by exciting the D_1 line of cesium atoms confined to an extremely thin cell (ETC), whose walls are separated by less than 1 μm, and developed an improved theoretical model to describe these signals with experimental precision. The theoretical model was based on the optical Bloch equations and included all neighboring hyperfine transitions, the mixing of the magnetic sublevels in an external magnetic field, and the Doppler effect, as in previous studies. However, in order to model the extreme conditions in the ETC more realistically, the model was extended to include a unified treatment of transit relaxation and wall collisions with relaxation rates that were obtained directly from the thermal velocities of the atoms and the length scales involved. Furthermore, the interactions of the atoms with different regions of the laser beam were modeled separately to account for the varying laser beam intensity over the beam profile as well as saturation effects that become important near the center of the beam at the relatively high laser intensities used during the experiments in order to obtain measurable signals. The model described the experimentally measured signals for laser intensities for magnetic fields up to 55 G and laser intensities up to 1 W/cm^2 with excellent agreement.

DOI: 10.1103/PhysRevA.91.023410 PACS number(s): 32.60.+i, 32.80.Xx, 32.10.Fn

I. INTRODUCTION

Modern fabrication techniques and technological requirements have led to a growing demand for smaller and smaller atomic vapor cells [1]. These "labs-on-a-chip" find applications in distributed atomic clocks that are required for precise global positioning, among other applications. Furthermore, extremely thin cells (ETCs) [2], one of whose dimensions can be as thin as several tens of nanometers, have found applications in fundamental research because they allow sub-Doppler spectroscopy without the need for expensive or complicated setups such as atomic beams or magneto-optical traps [3].

Such small vapor cells present particular challenges to theoreticians who wish to model the experimental signals. For one, relaxation rates are extremely high as a result of collisions with walls. Furthermore, since the volume of vapor interacting with the laser radiation in the thin cell is very small and thus contains fewer atoms than usual, experiments are usually performed at high temperature and/or laser intensity. In the former case, reabsorption may begin to play a role. In the latter case, the atom-laser interaction becomes saturated in the central regions of the beam, which means that the transit relaxation cannot be described any longer by an exponential with a single decay constant [4].

In this study, we aim to show that a precise description of magneto-optical signals in an ETC can be obtained with a theoretical model that is based on the optical Bloch equations extended to include a more detailed treatment of relaxation processes and the saturation of the atom-laser interaction in the high-intensity areas of the beam. We focused our study on the magneto-optical resonances, which are closely related to the ground-state Hanle effect, first observed in cadmium [5]. These resonances can be observed when at zero magnetic field a dark superposition state that does not absorb laser radiation forms among various degenerate ground-state magnetic sublevels [6–8]. This coherent dark state is destroyed when a magnetic field is applied, leading to an increase of absorption and laser-induced fluorescence (LIF). So-called dark resonances had been described earlier in alkali-metal atoms [9,10]. The Bloch equations were first applied to modeling dark resonances in a sodium beam [11]. In the linear regime at low powers analytical descriptions of such resonances are possible [12]. However, as the absorption of laser radiation becomes nonlinear, numerical models are normally used, and over time these models have been extended to include the coherent properties of the exciting laser radiation, the simultaneous interaction of all hyperfine sublevels in the ground and excited states with the laser radiation, magnetic-field-induced mixing of magnetic sublevels, and the Doppler effect [13]. These magneto-optical resonances provide a good test case for theoretical models as they include a wide range of coherent and incoherent processes [14].

Optical signals obtained with ETCs, where alkali-metal vapor is confined between two YAG crystals separated by a few hundred nanometers, present interesting properties related to the small dimension of the cell in the direction along a laser beam that is perpendicular to the ETC walls. Early efforts to model these signals focused on the Dicke-type narrowing observed in transmission signals when the wall separation was equal to an odd number of half wavelengths [15]. However, for fluorescence signals, this effect is not expected to be significant [16]. The effect of energy shifts induced by van der Waals interactions with the walls was considered, and for the cesium D_1 line could lead to shifts of the excitation maximum by up to 200 MHz for cell thicknesses around 50 nm [17]. Some of these early studies also applied the optical Bloch equations to a simplified two-level representation with optical pumping losses [15,18], but only in the linear excitation regime for intensities up to several milliwatts per square centimeter and

---

[*] marcis.auzins@lu.lv

Rabi frequencies less than 10 MHz. More recently, the cesium D_2 line has been studied experimentally and theoretically at somewhat higher powers up to 40 mW/cm^2 using a model based on the optical Bloch equations [19,20], but these models still were based on an open two-level system rather than including all degenerate sublevels. Furthermore, theoretical results were not compared directly to experimental curves, with the exception of some aggregate parameters, such as peak amplitude.

More sophisticated models were applied to describe experimentally measured magneto-optical signals obtained for the cesium D_2 [21] and rubidium D_1 [22] lines for atoms in ETCs, including all degenerate hyperfine levels of the excited- and ground-state manifolds. However, the proper treatment of collisions remained difficult and somewhat contradictory. The study of cesium atoms postulated a model for elastic collisions that redistributed the excited-state populations with weights that depended on the transition strength. In contrast, the study of rubidium atoms excluded these elastic collision terms and focused only on relaxation that was based on wall collisions. However, the best agreement between experiment and theory could be obtained only when different collisional relaxation rates were assumed for the ground and excited states.

We now applied a theoretical model to describe fluorescence signals of magneto-optical resonances that built on the previous efforts and added a more comprehensive approach towards treating properly saturation effects that are important for intense laser radiation whose power density varies over the beam profile. As in previous studies, the Bloch equations were applied, and all degenerate sublevels were included. The mixing of magnetic sublevels in an external magnetic field was also included, because this becomes important for magnetic fields of several tens of gauss or more. The equations were solved for various velocity groups and averaged over the residual Doppler profile. The equations contained relaxation terms for wall collisions and transit relaxation that were derived from the thermal velocities and the dimensions of the cell and the laser beam.

The additional feature included in the model this time to account for saturation effects and the varying laser intensity over the beam profile consisted in dividing the laser beam into concentric rings, and solving the Bloch equations separately for each ring, summing up the results with the appropriate weights. The particle exchange due to thermal motion between these concentric regions was included in the theoretical description. This final addition to the model was crucial to improving substantially the agreement between experimentally measured signals and the theoretical curves for magnetic field values up to at least 55 G, and it is a step towards resolving an outstanding problem in the modeling of magneto-optical signals [13].

In this article we present measurements of magneto-optical resonances recorded for cesium atoms confined to an ETC. Resonances have been recorded for all transitions of the D_1 line of cesium. In contrast to the complexity of the Rb D_1 or D_2 lines, the Cs D_1 line is much simpler. In this system, the increased hyperfine splitting and the presence of only one isotope make possible the investigation of individual hyperfine transitions. The ground-state hyperfine splitting is over 9 GHz and the excited-state hyperfine splitting is 1.17 GHz (see Fig. 1), markedly exceeding the Doppler width. The temperature dependence of the resonance shapes has been studied for temperatures up to 165 °C. Furthermore, the dependence of the resonance shapes on laser power and ETC wall separation have been studied. The extended theoretical model has been applied to describe the experimental signals, with excellent results.

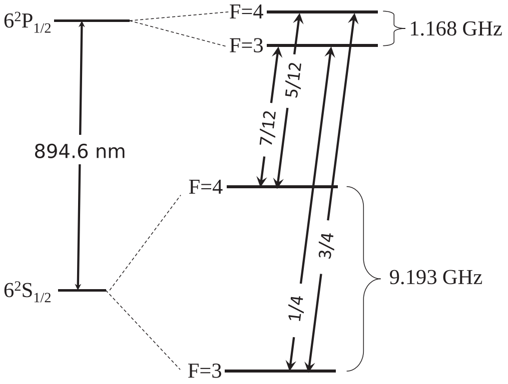

FIG. 1. Hyperfine level structure and transitions of the D_1 line of cesium (not to scale). The fractions on the arrows indicate the relative transition strengths.

II. EXPERIMENT

The ETC [2] consists of two YAG crystal windows that are glued together in such a way that the distance between them varies from 50 nm to 1.2 μm. It was produced at the Institute of Physical Research in Ashtarak, Armenia. The cesium is stored in a separate reservoir that is connected to the bottom part of the ETC. An additional thermocouple is attached to the cesium container for temperature measurements. For a more detailed description see [2].

In this experiment we performed magnetic-field scans over the zero-field resonance up to 55 G and detected the fluorescence signal from the ETC. We measured zero-field resonances for all four possible transitions of the Cs D_1 line (see Fig. 1). The experimental setup is shown in Fig. 2.

To control the temperature within the ETC and increase the vapor pressure, the cell was positioned inside a small oven. This oven was heated by a current that flowed through a bifilar coil in opposite directions to allow heating without producing stray magnetic fields. The oven consisted of two separate heating elements, which made it possible to maintain the cell itself and the cesium container at different temperatures. The cell's temperature was maintained at about 195 °C, while the temperature of the reservoir was varied between 70 °C and 165 °C. Both the cell and the oven were placed on top of a Thorlabs NanoMax table, which allowed precise three-dimensional (3D) positioning through three computer-controlled motors, each offering 4 mm of scan range. This setup was positioned at the center of three pairs of Helmholtz coils. Two coils were used to compensate the ambient magnetic field, and the third coil was used to scan the magnetic field up to 55 G by applying a current from a Kepco BOP-50-8-M bipolar power supply, which was controlled by a TTI TG5011 function generator.

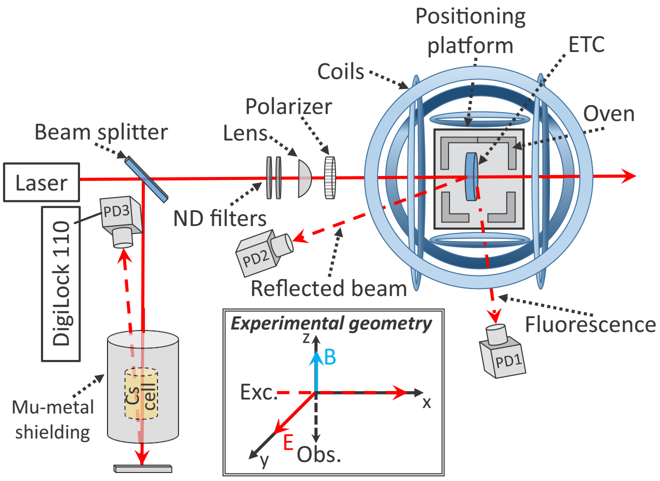

FIG. 2. (Color online) Schematic representation (top view) of the experimental setup.

The atoms were excited by a diode laser (DL100-DFB) from Toptica, AG, based on a distributed-feedback laser diode appropriate for exciting the D_1 line of cesium. The laser beam was split into two beams by a beam splitter. The weaker laser beam was directed to the cesium reference cell that was placed inside a three-layer μ-metal shield to eliminate the magnetic fields. The saturation absorption signal from the reference cell [measured by photodiode PD3 (Fig. 2)] was used in conjunction with the Toptica feedback controller DigiLock 110 for laser frequency stabilization.

The laser beam power was adjusted using a series of neutral-density filters, and the laser beam was focused onto the ETC with a lens whose focal length was 50 cm. The laser beam diameter was measured to be approximately 200 μm. Linear polarization of the laser beam (electric-field vector $\boldsymbol{E}$ in Fig. 2) was achieved with a Glan-Thompson polarizer (Thorlabs GTH10M). Because the glue reduces the amount of light that can pass through the side of the ETC, the fluorescence signal from the ETC was collected in a direction that made a small angle with the ETC cell walls and was focused using a series of lenses onto photodiode PD1 (Thorlabs FDS100). The lens system was constructed in such a way that it collected the fluorescence signal from only a small region, ignoring most of the scattered light from the cell walls.

The intensity of the beam reflected back from the second wall of the ETC was measured using photodiode PD2 (Thorlabs PDA36A-EC). The measured intensity was used to detect the interference spectrum, which, in turn, was used to determine the cell thickness. The voltage signals from the photodiodes were recorded using digital oscilloscopes (Yokogawa DL-6154 and Tektronix TDS 2004B).

III. THEORY

The basic approach of our theoretical description of magneto-optical signals has previously been described in [13] for ordinary vapor cells and expanded for the case of ETCs in [22]. In this section we describe how we extend the theoretical model to include a better description of the effects of transit relaxation and atom-wall collisions.

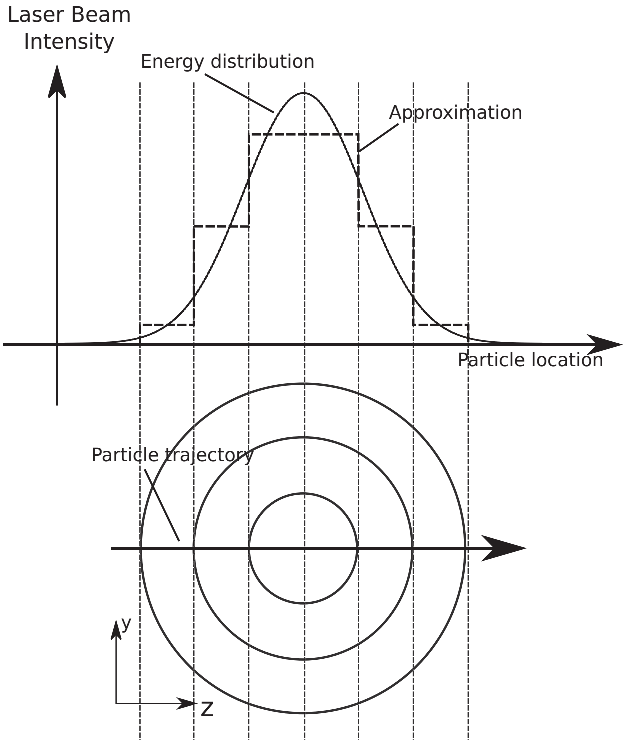

FIG. 3. Laser beam profile split into a number of concentric regions.

To derive rate equations that take into account the energy distribution within the laser beam profile, we assume that the particles move thermally, and their trajectories take them from outside the laser beam interaction region through the center of the laser beam. Assuming that all particles traverse the beam center is somewhat simplistic. At the cost of additional computing time, one could average also over off-center trajectories. In this case, however, such an additional averaging was not performed after our own tests showed that taking into account the different trajectories changed the results only negligibly in the ETC, probably because the effect of wall collisions was much more important. For the purposes of this derivation we will assume that the laser beam is directed along the x axis (Fig. 2 inset), which means that particle movement can be split into two cases: movement in the x direction, which accounts for Doppler broadening, and movement in the yz plane, which accounts for transit relaxation. Even though particles in the yz plane move in random directions, the axial symmetry of the laser beam allows us to describe them with a single trajectory for which the particle enters the laser beam from one side, moves along the z axis, and exits through the other side (Fig. 3).

To include the energy distribution of the laser beam in our model we split the z axis into multiple regions, giving each region its characteristic laser beam intensity (Fig. 3). This means that rate equations have to be written and solved for each region separately, giving a separate density matrix for each one.

To derive the rate equations for a single region we start with the rate equations for the density matrix ρ under the action of a Hamiltonian $\hat{H}$ and relaxation operator $\hat{R}$ in the following form:

$$i\hbar\frac{\partial\rho}{\partial t}=[\hat{H},\rho]+i\hbar\hat{R}\rho. \tag{1}$$

To include particles leaving and entering the interaction region we add the following terms to the right-hand side of the equation:

$$-i\hbar\hat{\gamma}_t\rho+i\hbar\hat{\gamma}_t\rho', \tag{2}$$

where ρ' is the density matrix of particles entering the region and $\hat{\gamma}_t$ is the transit relaxation operator, which can be written as a diagonal relaxation matrix with elements $\gamma_{tij}=v_{yz}/s_n\delta_{ij}$, where s_n is the region size, and v_{yz} is the characteristic particle speed. As we have assumed that all particles move in the same direction and transit regions sequentially, we can assume that for the nth region $\rho'=\rho^{(n-1)}$. By adding terms that describe collisional relaxation with rate γ_c, we arrive at rate equations for the density matrix $\rho^{(n)}$ of the nth region as

$$\begin{aligned}i\hbar\frac{\partial\rho^{(n)}}{\partial t}&=[\hat{H},\rho^{(n)}]+i\hbar\hat{R}\rho^{(n)}-i\hbar\hat{\gamma_t}^{(n)}\rho^{(n)}\\&\quad+i\hbar\hat{\gamma_t}^{(n)}\rho^{(n-1)}-i\hbar\hat{\gamma}_c\rho^{(n+i)}\hbar\hat{\gamma}_c\rho^0,\end{aligned} \tag{3}$$

where $\rho^{(0)}$ is the density matrix for atoms that do not interact with the laser radiation: their population is equally distributed among the ground-state sublevels. For atoms in the ETC there are two sources of collisional relaxation: atom-atom collisions and atom-wall collisions. To include both effects in the theoretical model, we write the collision relaxation operator as a diagonal matrix with elements:

$$\gamma_c=\frac{\bar{v}}{\bar{l}}+\frac{v_x}{L/2}, \tag{4}$$

where $\bar{v}$ is the mean atomic velocity, $\bar{l}$ is the mean free path, v_x is the atomic velocity in the direction perpendicular to the cell walls, and L is the cell thickness. The mean free path $\bar{l}={}^{\bar{v}}/_{\Gamma_{SE}}$, where $\bar{v}$ is the mean thermal velocity of the cesium atoms, and the rate of spin exchange $\Gamma_{SE}=\sigma_{SE}\bar{v}_{rel}n_a$, where $\sigma_{SE}=2.2\times10^{-14}$ cm^2 is the spin-exchange cross section [23], $\bar{v}_{rel}=({}^{8k_BT}/_{\pi\mu_{Cs}})^{1/2}$ is the average relative velocity of the cesium atoms (μ_{Cs} is the reduced mass of the system of two cesium atoms), and n_a is the density of atoms in the cell. At the temperatures studied here, the rate of atom-atom collisions is small compared to that of atom-wall collisions.

By following the derivation of rate equations for Zeeman coherences described earlier [24] and neglecting transit relaxation of optical coherences we arrive at the following differential equations:

$$\begin{aligned}\frac{\partial\rho^{(n)}_{g_i,g_j}}{\partial t}&=\sum_{e_k,e_m}\left(\Xi^{(n)}_{g_ie_m}+\left(\Xi^{(n)}_{e_kg_j}\right)^*\right)d^*_{g_ie_k}d_{e_mg_j}\rho^{(n)}_{e_ke_m}-\sum_{e_k,g_m}\left(\Xi^{(n)}_{e_kg_j}\right)^*d^*_{g_ie_k}d_{e_kg_m}\rho^{(n)}_{g_mg_j}-\sum_{e_k,g_m}\Xi^{(n)}_{g_ie_k}d^*_{g_me_k}d_{e_kg_j}\rho^{(n)}_{g_ig_m}\\&\quad-i\omega_{g_ig_j}\rho^{(n)}_{g_ig_j}+\sum_{e_ke_l}\Gamma^{e_ke_l}_{g_ig_j}\rho^{(n)}_{e_ke_l}-\gamma_t\rho^{(n)}_{g_ig_j}+\gamma_t\rho^{(n-1)}_{g_ig_j}-\gamma_c\rho^{(n)}_{g_ig_j}+\gamma_c\rho^{(0)}_{g_ig_j},\end{aligned} \tag{5}$$

$$\begin{aligned}\frac{\partial\rho^{(n)}_{e_i,e_j}}{\partial t}&=\sum_{g_k,g_m}\left(\left(\Xi^{(n)}_{e_ig_m}\right)^*+\Xi^{(n)}_{g_ke_j}\right)d^*_{e_ig_k}d_{g_me_j}\rho^{(n)}_{g_kg_m}-\sum_{g_k,e_m}\Xi^{(n)}_{g_ke_j}d_{e_ig_k}d^*_{g_ke_m}\rho^{(n)}_{e_me_j}-\sum_{g_k,e_m}\left(\Xi^{(n)}_{e_ig_k}\right)^*d_{e_mg_k}d^*_{g_ke_j}\rho^{(n)}_{e_ie_m}\\&\quad-i\omega_{e_ie_j}\rho^{(n)}_{e_ie_j}-\Gamma\rho^{(n)}_{e_ie_j}-\gamma_t\rho^{(n)}_{e_ie_j}+\gamma_t\rho^{(n-1)}_{e_ie_j}-\gamma_c\rho^{(n)}_{e_ie_j},\end{aligned} \tag{6}$$

where

$$\Xi_{g_ie_j}=\frac{|\boldsymbol{\varepsilon}^{(n)}|^2}{\frac{\Gamma+\Delta\omega}{2}+i\left(\bar{\omega}-kv_x+\omega_{g_ie_j}\right)} \tag{7}$$

characterizes the laser beam interaction with $|\boldsymbol{\varepsilon}^{(n)}|^2$, which is proportional to the laser beam intensity of the nth region, Γ is the spontaneous relaxation rate, $\Delta\omega$ is the spectral width of the laser beam, $\bar{\omega}$ is the laser frequency, kv_x is the Doppler shift for light with wave vector k propagating in the x direction, $\omega_{g_ie_j}$ is the energy difference between the ground-state magnetic sublevel g_i and the excited-state magnetic sublevel e_j, and $d_{g_ie_j}$ and $d_{e_jg_i}$ are the dipole transition matrix elements that couple the excited- and ground-state magnetic sublevels. In order to relate the dipole strengths to laser intensity more conveniently, we can introduce the reduced Rabi frequency as $\Omega_R=\boldsymbol{\varepsilon}'_r/\hbar$, where $\boldsymbol{\varepsilon}'_r$ is the electric-field intensity at the center of the laser beam and d is the reduced matrix element of the dipole transition obtained from the matrix elements of $d_{e_jg_i}$ when the Wigner-Eckart theorem is applied [24]. Because the equations include a term for particle speed, the subsequent averaging of the fluorescence signal over the Maxwell distribution in the direction of the laser beam is needed to include Doppler shifts. An extra averaging over the v_{yz} plane can be applied for the averaged transit relaxation, but the relative gains in precision are negligible at the laser powers of interest to us compared to the additional time required for the calculations. As the relaxation process dynamics are included in the transit relaxation terms, the calculations can be done for the steady state by solving a system of linear equations for density matrix ρ that in turn can be used to calculate the fluorescence intensity $I(\boldsymbol{\varepsilon}_f)$ where $\boldsymbol{\varepsilon}_f$ is the fluorescence polarization.

In the end the fluorescence signal for polarization $\boldsymbol{\varepsilon}_f$ can be expressed as

$$I(\boldsymbol{\varepsilon}_f)=\sum_n\sum_{v_x}f(v_x)\Delta v_x\frac{A_n}{A}I_n(v_x,\boldsymbol{\varepsilon}_f), \tag{8}$$

where n runs over the regions in the direction of the particle trajectory, v_x is the particle speed in the direction of the laser beam, $f(v_x)\Delta v_x$ is the probability of finding atoms with velocity $v_x\pm{}^{\Delta v_x}/_2$, ${}^{A_n}/_A$ is the relative area of region n, and

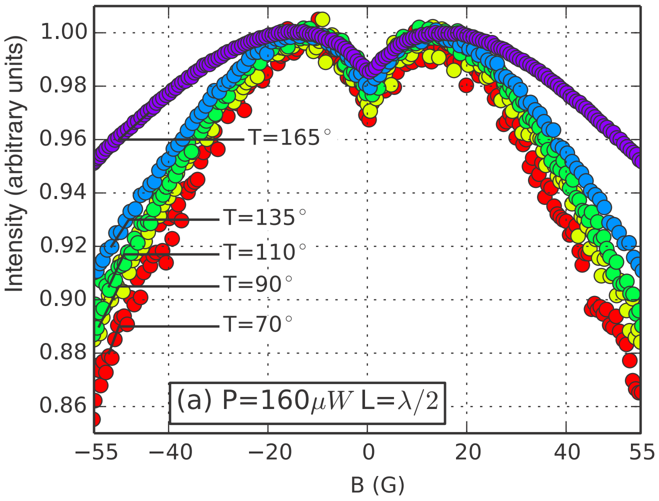

FIG. 4. (Color online) Signal dependence on temperature for the $F_g = 4 \rightarrow F_e = 4$ transition at a cell wall separation of approximately 450 nm.

$I_n(v_x, \boldsymbol{\varepsilon}_f)$ is the fluorescence intensity of the nth region with atomic velocity v_x in laser beam direction.

IV. RESULTS AND DISCUSSION

To analyze the effects of the ETC on magneto-optical signals we began by measuring the temperature dependence of the Cs D_1 $F_g = 4 \rightarrow F_e = 4$ transition for a wall separation of $L = \lambda/2$ and a constant laser power P of 160 μW, which corresponds to an average power density of 500 mW/cm^2 for a laser beam diameter of 0.2 mm. The experimental results are shown in Fig. 4. It can be seen that the fluorescence signal recorded at 165 °C significantly deviates from signals obtained at lower temperatures. The effect can be explained by the rapid vapor pressure rise in the cell, which eventually leads to reabsorption effects becoming important. Indeed, using the resonant cross section of the D_1 line for π-polarized radiation and the density of cesium at 165 °C [25] one obtains an optical path length of 1.5 μm, which becomes comparable to the cell thickness and corresponds to an optical depth (OD) of 0.6. At similar optical depths (OD of approximately 0.66), reabsorption effects have been observed to start to play a role in an ordinary cell [26,27]. To study ETC effects without the added complication of reabsorption, we chose to conduct experiments at a temperature in the cesium reservoir of 90 °C, at which the optical absorption length is greater than 80 μm. At this temperature reabsorption effects were still negligible, but the fluorescence signal was detectable even at low laser power.

Figure 5 shows the shapes of the fluorescence signal together with theoretical curves for all four D_1 transitions at a constant laser power of 160 μW and a wall separation that is equal to the wavelength of the laser radiation. The laser beam diameter, laser power, laser wavelength, and cell temperature were directly measured from the experiment. The Rabi frequency was adjusted in order to obtain the best overall fit. The calculations were performed by dividing the beam into $N = 20$ regions.

On analyzing Fig. 5, as expected, we can see three dark resonances for transitions $F_g = 3 \rightarrow F_e = 3$ and $F_g = 4 \rightarrow F_e = 3,4$. For the transition $F_g = 3 \rightarrow F_e = 4$ a bright resonance would be expected in an ordinary cell, but the experimental and theoretical results show no bright resonance

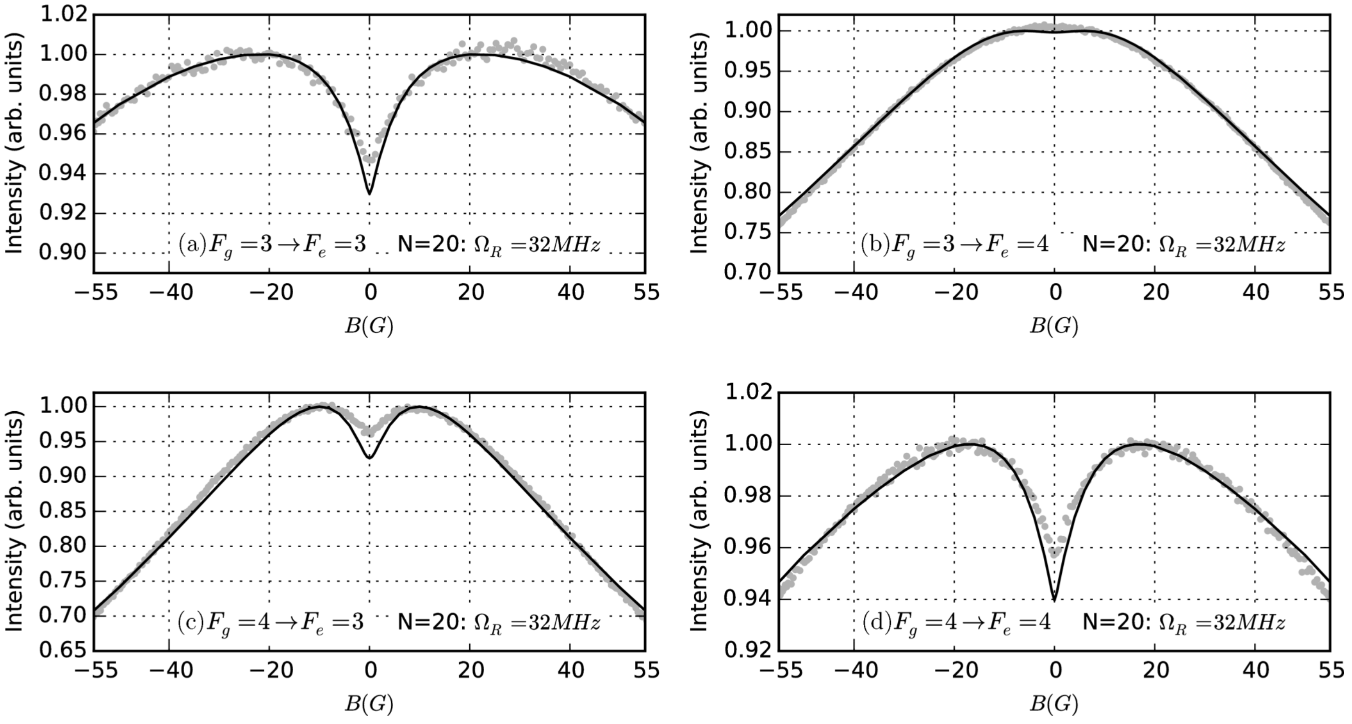

FIG. 5. Magneto-optical resonances for different D_1 transitions at laser power of 160 μW and wall separation $L = \lambda$. (Gray dots, experiment; solid line, theory.)

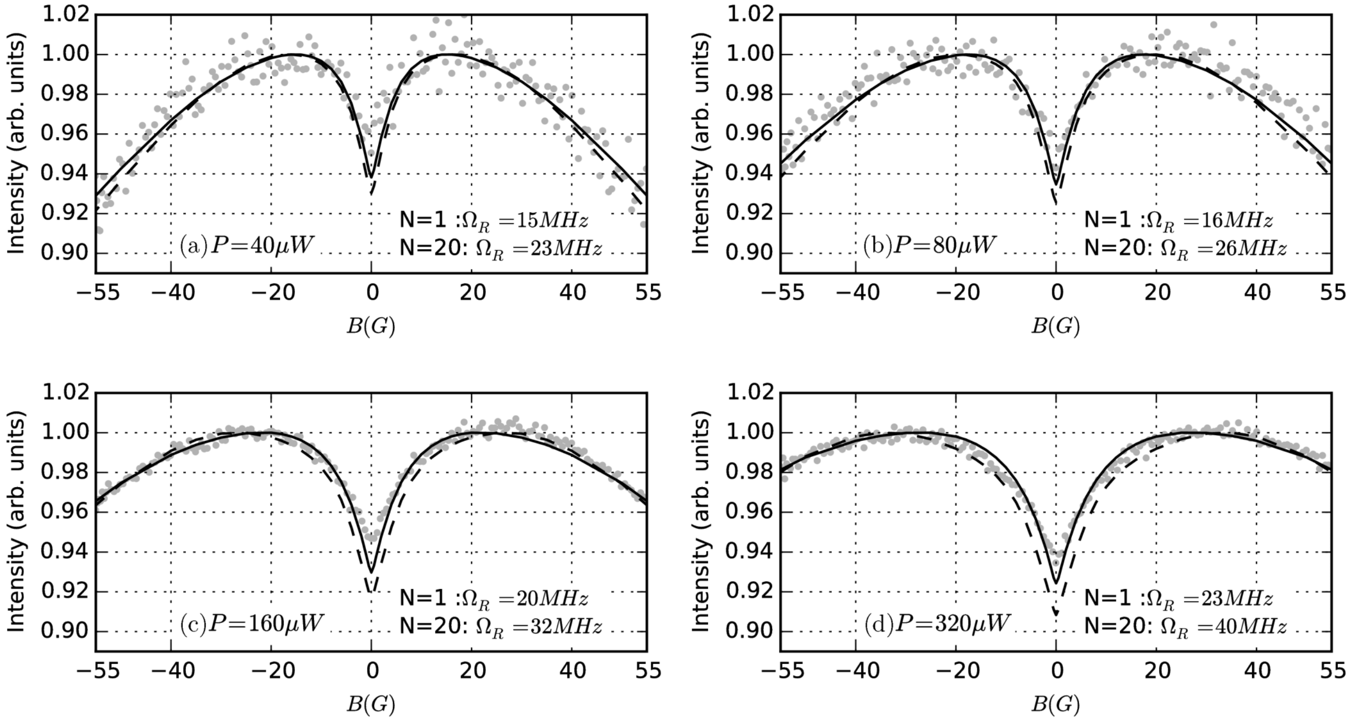

FIG. 6. Power dependence of the $F_g = 3 \rightarrow F_e = 3$ transition compared to different theories (dots, experiment; dashed line, one-region model; solid line, 20-region model).

in the ETC. The bright resonance, for which the lowest contrast is expected, is destroyed by the rapid relaxation due to atom-wall collisions. This behavior had been observed already experimentally in rubidium atoms confined to an ETC [22].

Next we turned our attention to the power dependence of the resonance shapes. Figure 6 shows such a dependence for the $F_g = 3 \rightarrow F_e = 3$ transition. To compare results of the improved description of transit relaxation with those obtained from a simpler treatment, two theoretical curves are given in each subfigure. One curve has been calculated assuming that the laser beam was characterized by a single power density ($N = 1$). To calculate the other curve, the laser beam was assumed to be of Gaussian shape and split into 20 regions ($N = 20$) of equal width (see Fig. 3). The number of regions was chosen in such a way that the results of theoretical calculations converged with further subdivisions resulting in negligible changes in the fluorescence signal. In fact, a calculated curve for another transition with $N = 20$ differed from the curve with $N = 10$ by only 10^{-3} in the units used in our figures. The same value of 32 MHz was used as the reduced Rabi frequency in the central region for all transitions. The reduced Rabi frequency was modified for each transition according to its line strength. By comparing the results of the theoretical models, one can see that the theoretical curve of the single-region model agrees well with experimental measurements for cases where the laser power is low, but starts to deviate significantly in cases where the laser power is higher. This behavior has already been observed experimentally numerous times in ordinary cells ([13,14,26,28]) where theoretical calculations start to deviate from experimental data at laser powers where absorption at the center of the laser beam has reached saturation. In the case of the ETC even the lowest laser power used is noticeably higher than laser powers used in ordinary cell experiments, but, because of the strong relaxation by collisions with cell walls, noticeable deviations from experimental results start at only very high laser power densities. At such powers, by including the laser beam profile in the theoretical model, the agreement between theoretical calculations and experimental results could be greatly improved, especially in the description of the broader structure at larger magnetic field values (see [22]).

Finally we examined the signal dependence on cell thickness L. The experimental results for $F_g = 4 \rightarrow F_e = 4$ together with theoretical calculations are shown in Fig. 7. The calculations were performed for $N = 20$ concentric regions, and the Rabi frequencies for theoretical calculations were fitted for each cell thickness. The reason for tuning the Rabi frequencies was the fact that different thickness measurements were performed in different parts of the cell, for which the cell wall transparency may have been somewhat different.

It can be seen that the contrast of the zero-field resonance changes only by about 2% while the power density is increased by a factor of 8 (Fig. 6). At the same time it can be seen that the contrast of the magneto-optical signal is governed by the temperature (Fig. 4) and cell thickness (Fig. 7) rather than by the laser power.

V. CONCLUSIONS

ETCs are different from ordinary cells because collisions with walls play a much larger role in contrast to ordinary cells, where transit relaxation effects usually dominate over wall-to-wall collisions even at moderate laser powers. In order to improve the theoretical description of magneto-optical signals in ETCs, the theoretical model was extended to include

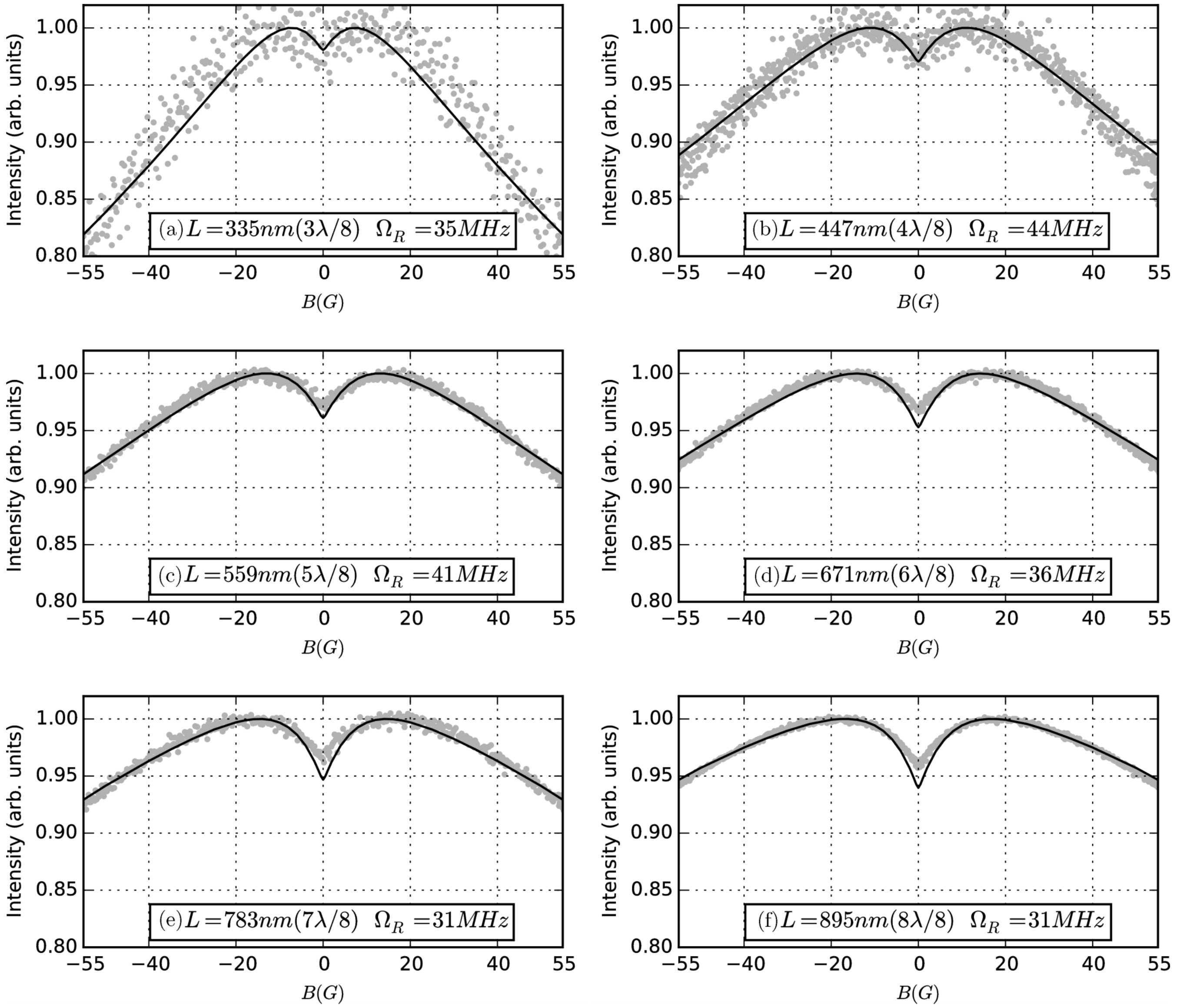

FIG. 7. Magneto-optical resonance signal shape at different ETC cell thickness for the transition $F_g = 4 \rightarrow F_e = 4$. (Dots, experiment; solid line, theory.)

the intensity distribution in the cross section of the laser beam and to treat collisions carefully. As a result, measured nonlinear magneto-optical resonances for the Cs D_1 line for magnetic-field values up to at least 55 G can be described much more precisely than before. Such a model could be very useful in improving the description of magneto-optical signals in ordinary cells at laser power densities that may be found in typical experiments. Indeed, since the relaxation rate for wall collisions in an ordinary cell is several orders of magnitude smaller than in an ETC, the division of the laser beam into various regions should yield even greater benefits, which we will discuss in a separate presentation.

ACKNOWLEDGMENTS

The Riga group gratefully acknowledges financial support from the Latvian National Research Programme (VPP) project IMIS^2.

---

[1] R. Mhaskar, S. Knappe, and J. Kitching, A low-power, high-sensitivity micromachined optical magnetometer, Appl. Phys. Lett. **101**, 241105 (2012).

[2] D. Sarkisyan, D. Bloch, A. Papoyan, and M. Ducloy, Sub-Doppler spectroscopy by sub-micron thin Cs vapour layer, Opt. Commun. **200**, 201 (2001).

[3] A. Sargsyan, G. Hakhumyan, A. Papoyan, D. Sarkisyan, A. Atvars, and M. Auzinsh, A novel approach to quantitative spectroscopy of atoms in a magnetic field and applications based on an atomic vapor cell with $L = \lambda$, Appl. Phys. Lett. **93**, 021119 (2008).

[4] M. P. Auzin'sh, R. S. Ferber, and I. Ya. Pirags, K_2 ground-state relaxation studies from transient process kinetics, J. Phys. B: At. Mol. Phys. **16**, 2759 (1983).

[5] J. C. Lehmann and C. Cohen-Tannoudji, Pompage optique en champ magnétique faible, C. R. Acad. Sci. (Paris) **258**, 4463 (1964).

[6] A. P. Kazantsev, V. S. Smirnov, A. M. Tumaikin, and I. A. Yagofarov, Effect of atomic ground state self-polarization in the optical pumping cycle on the increase of linear light absorption for $j \longrightarrow j+1$ transitions, Opt. Spectrosc. (USSR) **57**, 116 (1984).

[7] F. Renzoni, S. Cartaleva, G. Alzetta, and E. Arimondo, Enhanced absorption Hanle effect in the configuration of crossed laser beam and magnetic field, Phys. Rev. A **63**, 065401 (2001).

[8] J. Alnis and M. Auzinsh, Angular-momentum spatial distribution symmetry breaking in Rb by an external magnetic field, Phys. Rev. A **63**, 023407 (2001).

[9] R. W. Schmieder, A. Lurio, W. Happer, and A. Khadjavi, Level-crossing measurement of lifetime and hfs constants of the ${}^2P_{3/2}$ states of the stable alkali atoms, Phys. Rev. A **2**, 1216 (1970).

[10] G. Alzetta, A. Gozzini, L. Moi, and G. Orriols, An experimental method for the observation of r.f. transitions and laser beat resonances in oriented Na vapour, Nuovo Cimento B **36**, 5 (1976).

[11] J. L. Picqué, Hanle effect in an atomic beam excited by a narrow-band laser, J. Phys. B: At. Mol. Phys. **11**, L59 (1978).

[12] E. Breschi and A. Weis, Ground-state Hanle effect based on atomic alignment, Phys. Rev. A **86**, 053427 (2012).

[13] M. Auzinsh, R. Ferber, F. Gahbauer, A. Jarmola, and L. Kalvans, F-resolved magneto-optical resonances in the D_1 excitation of cesium: Experiment and theory, Phys. Rev. A **78**, 013417 (2008).

[14] M. Auzinsh, A. Berzins, R. Ferber, F. Gahbauer, L. Kalvans, and A. Mozers, Coherent and incoherent processes responsible for various characteristics of nonlinear magneto-optical signals in rubidium atoms, J. Phys. B: At. Mol. Opt. Phys. **46**, 185003 (2013).

[15] G. Dutier, S. Saltiel, D. Bloch, and M. Ducloy, Revisiting optical spectroscopy in a thin vapor cell: Mixing of reflection and transmission as a Fabry-Perot microcavity effect, J. Opt. Soc. Am. B **20**, 793 (2003).

[16] I. Maurin, P. Todorov, I. Hamdi, A. Yarovitski, G. Dutier, D. Sarkisyan, S. Saltiel, M.-P. Gorza, M. Fichet, D. Bloch, and M. Ducloy, Probing an atomic gas confined in a nanocell, J. Phys.: Conf. Ser. **19**, 20 (2005).

[17] I. Hamdi, P. Todorov, A. Yarovitsky, G. Dutier, I. Maurin, S. Saltiel, Y. Li, A. Lezama, T. Varzhapetyan, D. Sarkisyan, M.-P. Gorza, M. Fichet, D. Bloch, and M. Ducloy, Laser spectroscopy with nanometric gas cells: Distance dependence of atom-surface Interaction and collisions under confinement, Laser Phys. **15**, 987 (2005).

[18] A. D. Sargsyan, D. H. Sarkisyan, Y. Pashayan-Leroy, C. Leroy, P. Moroshkin, and A. Weis, Dependence of the cesium absorption D_1 linewidth on the thickness of the atomic vapor column, J. Contemp. Phys. (Arm. Acad. Sci.) **43**, 7 (2008).

[19] C. Andreeva, S. Cartaleva, L. Petrov, S. M. Saltiel, D. Sarkisyan, T. Varzhapetyan, D. Bloch, and M. Ducloy, Saturation effects in the sub-Doppler spectroscopy of cesium vapor confined in an extremely thin cell, Phys. Rev. A **76**, 013837 (2007).

[20] S. Cartaleva, A. Krasteva, L. Moi, A. Sargsyan, D. Sarkisyan, D. Slavov, P. Todorov, and K. Vaseva, Laser spectroscopy of sub-micrometre- and micrometre-thick caesium-vapour layers, Quantum Electron. **43**, 875 (2013).

[21] C. Andreeva, A. Atvars, M. Auzinsh, K. Blush, S. Cartaleva, L. Petrov, and D. Slavov, Ground-state magneto-optical resonances in cesium vapour confined in an extremely thin cell, Phys. Rev. A **76**, 063804 (2007).

[22] M. Auzinsh, R. Ferber, F. Gahbauer, A. Jarmola, L. Kalvans, A. Papoyan, and D. Sarkisyan, Nonlinear magneto-optical resonances at D_1 excittaion of ^{85}Rb and ^{87}Rb in an extermely thin cell, Phys. Rev. A **81**, 033408 (2010).

[23] K. Ernst and F. Strumia, High efficiency hyperfine pumping of cesium vapor, Phys. Rev. **170**, 48 (1968).

[24] K. Blushs and M. Auzinsh, Validity of rate equations for Zeeman coherences for analysis of nonlinear interaction of atoms with broadband laser radiation, Phys. Rev. A **69**, 063806 (2004).

[25] D. A. Steck, Cesium D Line Data, http://steck.us/alkalidata/cesiumnumbers.pdf (revision 2.1.4, 23 December 2010).

[26] M. Auzinsh, A. Berzins, R. Ferber, F. Gahbauer, L. Kalvans, A. Mozers, and D. Opalevs, Conversion of bright magneto-optical resonances into dark resonances at fixed laser frequency for D_2 excitation of atomic rubidium, Phys. Rev. A **85**, 033418 (2012).

[27] A. B. Matsko, I. Novikova, and G. R. Welch, Radiation trapping under conditions of electromagnetically induced transparency, J. Mod. Opt. **49**, 367 (2002).

[28] M. Auzinsh, A. Berzins, R. Ferber, F. Gahbauer, L. Kalvans, A. Mozers, and A. Spiss, Dependence of the shapes of nonzero-field level-crossing signals in rubidium atoms on the laser frequency and power density, Phys. Rev. A **87**, 033412 (2013).

LATVIAN JOURNAL OF PHYSICS AND TECHNICAL SCIENCES
2015, N 3
DOI: 10.1515/LPTS-2015-0013

PHYSICS

MAGNETIC FIELD GRADIOMETER WITH SUB-MICRON SPATIAL RESOLUTION BASED ON CAESIUM VAPOUR IN AN EXTREMELY THIN CELL

M. Auzinsh[1], A. Berzins[1], R. Ferber[1], F. Gahbauer[1], U. Kalnins[1],
R. Rundans[1] and D. Sarkisyan[2]

[1]Laser Centre, the University of Latvia, 19 Rainis Blvd., Riga, LV-1586, LATVIA
[2]Institute for Physical Research, NAS of Armenia, Ashtarak-0203, ARMENIA
e-mail: andris.beerzinsh@gmail.com

In this paper we present a device for measuring the magnetic field and its gradient with a spatial resolution of several hundred nanometres. This device is based on caesium metal vapour confined to an extremely thin cell (ETC). To measure magnetic signals, we use absorption and very low laser powers, which might be appealing for modern fabrication techniques. A portable, fully automated device was constructed.

Keywords: *extremely thin cell, magnetometer, measurements of magnetic field gradient, magneto-optical resonances*.

1. INTRODUCTION

Atomic vapour magnetometers have many advantages, among which are their precision and high sensitivity. Additionally, atomic magnetometers do not require cryogenic cooling, they are insensitive to spatial rotation, and they offer a significant potential for miniaturisation. Moreover, they are faster than fluxgate magnetometers. As a result, magnetometers based on gaseous species are of interest not only in physics, but also in other fields. For example, in archaeology and geophysics a set of caesium magnetometers has shown better characteristics in speed, quality, and spatial resolution than the fluxgate magnetometers [1]. In biology, caesium magnetometers have proved themselves to be as good as or even better than superconducting quantum interference devices (SQUIDs) in terms of sensitivity when measuring magnetic field changes in plants [2]. In space exploration, devices based on atomic magnetometers have great potential due to their compact size, and spin exchange relaxation-free (SERF) atomic magnetometers have already demonstrated an unsurpassed, ultra-high sensitivity of $0.54\,\mathrm{fT\,Hz^{-1/2}}$ with a measurement volume of only $0.3\,\mathrm{cm^3}$ [3]. Developments in this technology can produce sensors that can be operated on a fully optical basis [4], i.e., input and output signals in form of light using optical waveguides. In such a way, magnetic field measurements could be done in places with strong electrical interference present. And finally, by detecting nuclear quadrupole resonance, atomic magnetometers can be used to detect dangerous or illegal substances, such as plastic explosives [5].

Nevertheless atomic magnetometers traditionally have relatively poor spatial resolution. Usually the distance between the walls of a standard spectroscopic cell is a few centimetres, or in the best case few millimetres [6], which also gives the approximate scale of achievable spatial resolution.

One way to achieve better spatial resolution is building a spectroscopy device based on an extremely thin cell (ETC). ETCs are spectroscopic cells that have two walls separated by a distance from 30nm up to several micrometres [7]. If the laser radiation propagates in the direction perpendicular to the ETC walls, most of the fluorescence will be observed from those atoms, whose velocity is small in the direction normal to the walls, since atoms flying rapidly toward an ETC wall will collide with it before being able to fluoresce. A picture of an ETC (Fig. 1) shows the interference pattern for visible light that results from the weak Fabry–Perot etalon created by the cell walls.

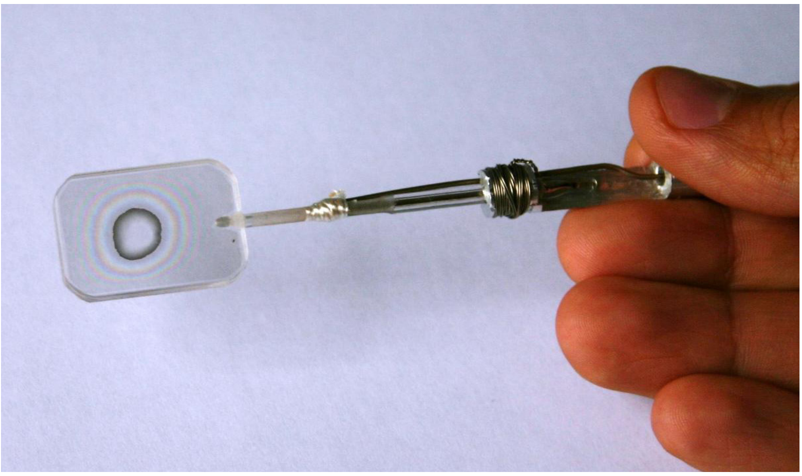

Fig. 1. A photo of ETC.

It is known that alkali metal vapours confined between walls separated by only a few hundred nanometres have the potential for applications in magnetic field measurements with elevated spatial resolution [8]. Furthermore, there is a large body of research about magneto-optical resonances (MORs) in alkali metal vapours in ordinary cells and in ETCs. For instance, nonlinear MORs have been studied experimentally and theoretically for D_1 excitation of atomic caesium, and the theoretical model [9] is successful for describing the resonances in detail [10]. Moreover, the theoretical model has proved itself by describing more complex systems with partially resolved hyperfine levels, such as the Rb D_1 and D_2 lines [11], [12], and it was in good agreement with experiments carried out in the ETC as well [13].

In this paper, we present a portable and fully automated magnetic field gradiometer with excellent characteristics in terms of spatial resolution. The device can be operated by a user without any physics training thanks to the simple-to-use software.

2 EXPERIMENTAL SETUP OF THE DEVICE

A schematic representation of the device is shown in Fig. 2. To excite the caesium atoms, we used a diode laser (Toptica DL100-DFB). A small fraction of the laser radiation was diverted from the main beam to obtain a saturation absorption (SA) spectrum in an ordinary Cs reference cell that was placed inside a three-layer mu-metal shield. The laser was stabilized to the peaks in the SA spectrum. The mu-metal shielding allowed the SA peaks to remain at fixed frequencies regardless of the magnetic field environment. Frequency stabilization was achieved by a Toptica "DigiLock 110" laser control unit, using an error signal derived from the SA spectrum. The main laser beam intensity was adjusted with a series of neutral density filters. The laser beam was focused on the extremely thin cell with a lens (f = 50 cm) and polarized with a Glan-Thompson polarizer (Thorlabs GTH10M).

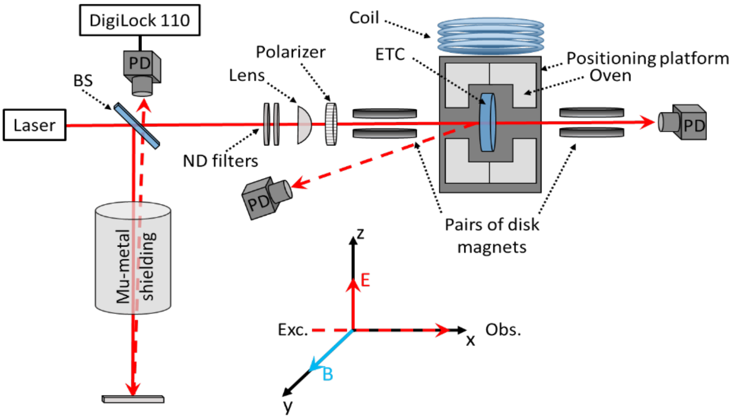

Fig. 2. Experimental setup of the device.

To achieve higher atomic density within the cell, the temperature was raised to 150°C using a small oven with bifilar heating coils to avoid generating additional fields. For the gradient measurements both the cell and the oven were mounted to a Thorlabs NanoMax positioning table, which offers a positioning resolution of 20 nm in three dimensions via voltage applied to piezo crystals. The cell position was controlled with a function generator (TTI TG5011). The absorption spectrum from the ETC was detected using a photodiode (Thorlabs PDA36-EC). The cell thickness was inferred from the interference maxima and minima in the beam reflected from the cell wall. The signals from the photodiodes were measured by a digital oscilloscope (Yokogawa DL-6154).

For the calibration of the absorption spectrum, an extra coil was added next to the oven, capable of producing a magnetic field up to 60 G. The current in the coils was produced by a bipolar power supply (Kepco BOP-50-8-M), which was controlled by another function generator (TTI TG5011). A magnetic field with a strong gradient was created around the ETC using four neodymium disk magnets.

The laser beam frequency was held constant at the $Cs\ D_1$ transition $F_g=4 \rightarrow F_e=3$, where F_g stands for quantum number of full atomic angular momentum of the ground state and F_e stands for quantum number of full atomic angular momentum of the excited state. The cell thickness was measured to be approximately 450 nm. The laser power was held at constant 5 μW with a beam diameter of 200 μm. The approximate magnetic field within the cell was from 10 G to 80 G, depending on the position. The cell was scanned over a distance of 15 μm in the direction of the laser beam with frequency of 51.4 mHz.

The dimensions of the completely assembled unit (Fig. 3) are 1.5x1x0.7 m.

Fig. 3. Completely assembled device. In the upper right part of the device one can see the optical system of the device (schematically in Fig. 2). In the left part of the device there is a PC with a monitor, keyboard, and mouse to operate the device. In the bottom right part of the device one can find power supplies, laser control units, scan generators and the positioning table control unit. All of the devices which tend to vibrate are isolated with soft plastic materials. The device is placed on a cart with wheels, which allowed it to be moved about the lab.

The measurement procedure was as follows. First, the absorption spectrum had to be calibrated. The calibration was done by scanning the magnetic field in the external coil with constant position and plotting the known magnetic field value against the absorption signal (Fig. 4). The resulting curve was fit with a fifth degree polynomial. The measurement of magnetic field gradient was done with coil turned off and the previously acquired calibration curve was then used for calculating the magnetic field values from the measured signal.

The measurement was fully computer controlled via the Virtual Instrument Software Architecture (VISA) interfaces of function generators and oscilloscope. Custom user-interface software was written for parameter input and automatisation of the calibration and measurement processes. The results of a typical measurement are shown in Fig. 5. The software allows the operator to choose the device, which will record the measurement – in our case the oscilloscope. It is possible to choose the scan generators controlling the coil and the piezo drives. There are two windows-calibration and magnetic gradient measurements. The device has default parameters for both measurements, but they can be alternated for faster or slower measurements, different scan ranges, and level of averaging. The software allows the user to save the current measurement and load the previous ones.

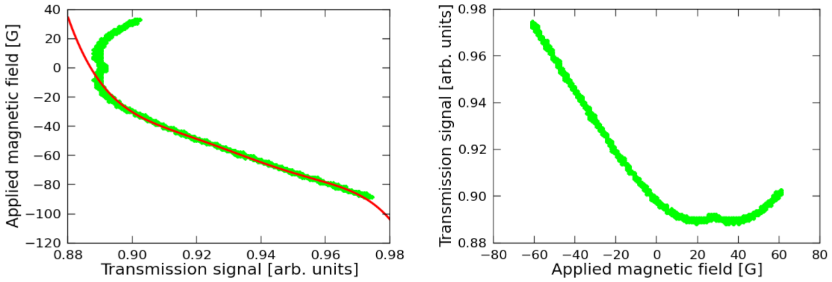

Fig. 4. Left panel – calibration signal, right panel – signal with the fitted curve, which is used to calculate magnetic field values for the gradient measurements.

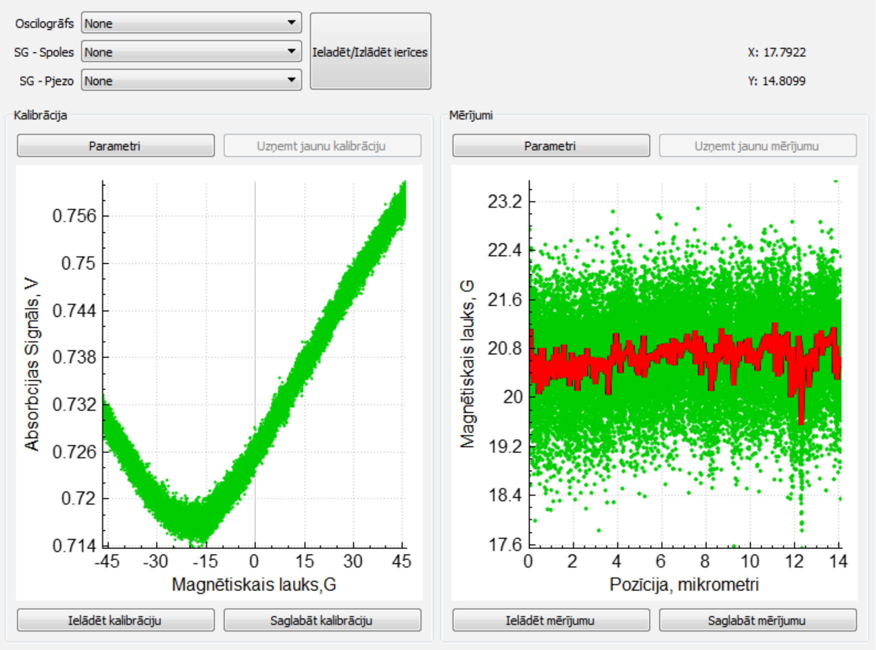

Oscilogrāfs: None
SG - Spoles: None
SG - Pjezo: None

X: 17.7922
Y: 14.8099

Fig. 5. Program window for measurement control. Left panel – calibration signal, right panel – magnetic field gradient measurement with one scan (blue dots), and averaged data (red line). *Note:* the red line represents the average of the measurements from one scan, not multiple scans.

3. RESULTS

By scanning the magnetic field with the coil, we get information about magnetic field values. Figure 6 shows a classical MOR with a narrow peak at zero magnetic field and rising wings at larger magnetic field values, which can be used for calibration. In Fig. 6 we can see that the zero-field resonance is reached at an applied field of approximately -30 G. From this measurement we can calibrate our gradient measurement. In this case one must remember that even with one coil we can get a homogeneous magnetic field in the cell because the region we observe is so small that the inhomogeneity is negligible compared to measurement resolution.

In Fig. 7 a magnetic gradient measurement with averaging over multiple scans is depicted. In this graph (Fig. 7) we present a 14 µm position scan, whose absorption signal is fitted with a straight line. From this graph one can see that there is a linear magnetic field gradient over these 14 µm with the value of ~2357 G/m. The linear dependence is expected based on the fact that MORs in ETC in alkali metal vapour at elevated magnetic field values show linear dependence on magnetic field changes.

Before measuring the magnetic field, we made a simple calculation to know what magnetic field value is expected at a certain distance from the magnets. After calculating the expected magnetic field values, we made multiple scans without changes in magnetic field (i.e., ETC position) and concluded that at a magnetic field of 74 G the uncertainty in measured magnetic field values was ± 0.3 G. This gives us an error for the magnetic field measurement of 0.4%. The tested sensitivity of magnetic gradient measurement with our device was 20 mG/µm, and the accuracy with which we could detect a magnetic field gradient was about 2 mG/µm.

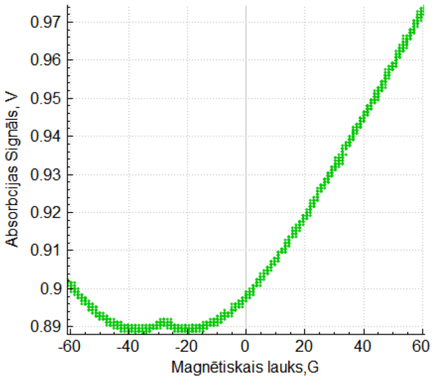

Fig. 6. Absorption signal (magneto-optical resonance) obtained for calibration.

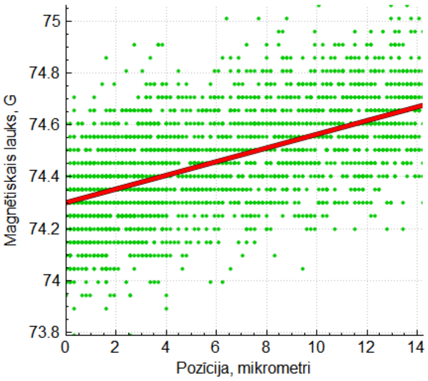

Fig. 7. Magnetic field gradient measurement (absorption signal).

4. CONCLUSIONS

Our device has proved that magnetometers on the basis of gaseous species can measure magnetic fields with outstanding spatial resolution. We have constructed a practical example for an optical magnetometer with submicron spatial resolution based on alkali metal vapours. It should be noted that the idea of using ETCs in magnetometers with outstanding spatial resolution was proposed in [7] and a laboratory device was constructed and presented in the same study. However, the device we present is portable and automated, which is the next step from a laboratory device.

With slight modifications in the system, it would be possible to measure even stronger magnetic fields. For example, a coil that can generate stronger magnetic fields could give precise calibration data for larger magnetic fields, enabling measurements at magnetic field values over 100 G. Measuring near-zero magnetic fields would require additional upgrades for the software, because the linear fit for the calibration data would not be appropriate for the MOR structure at low magnetic fields. However, absorption signals in the alkali metal vapour do undergo changes near-zero magnetic field, so there are no restrictions for measuring small magnetic fields from the viewpoint of physical processes.

It should be mentioned that the system can be further improved by reducing its size – it easily could be reduced to one fourth of its starting size (many of the power supplies and control units could be replaced by smaller ones and layout of the devices could be optimized). Measurement precision could be improved by adding an additional layer of thermal isolation. Additional vibration absorbers would reduce the measurement noise. It is also possible to make measurements even at smaller distances between cell walls, but it would require longer measurement times due to the fact that layer of atoms forming the absorption signal would be even thinner.

ACKNOWLEDGEMENTS

The contribution of Artis Kruzins to the construction of the device is highly appreciated. Riga group gratefully acknowledges support from ERDF (ERAF) project no. 2010/0242/2DP/2.1.1.1.0/10/APIA/VIAA/036 "New Technology for Magnetic Field and Its Gradient Measurements Using Nanostructured Gas Environment".

REFERENCES

1. Mathé, V., Lévêque, F., and Druez, M. (2009). What interest to use caesium magnetometer instead of fluxgate gradiometer? *Mémoire du sol, espace des homes*, *33* (suppl.), 325–327.
2. Corsini, E., Acosta, V., Baddour, N., Higbie, J., Lester, B., Licht, P., Patton, B., Prouty, M., and Budker, D. (2011). Search for plant biomagnetism with a sensitive atomic magnetometer. *J. Appl. Phys. 109*, 074701, DOI:10.1063/1.3560920.
3. Kominis, I.K., Kornack, T.W., Allred J.C., and Romalis, M.V. (2003). A subfemtotesla multichannel atomic magnetometer. *Nature 422*, 596–599, DOI: 10. 1038/nature01484.
4. Patton, B., Zhivun, E., Hovde, D.C., and Budker, D. (2014). All-optical vector atomic magnetometer. *Phys. Rev. Lett. 113*, 013001, DOI:10.1103/PhysRevLett.113.013001.
5. Lee, S.-K., Sauer, K.L., Seltzer, S.J., Alem, O., and Romalis, M.V. (2006). Subfemtotesla radio-frequency atomic magnetometer for detection of nuclear quadrupole resonance. *Appl. Phys. Lett. 89*, 214106, DOI:10.1063/1.2390643.
6. Balabas, M.V., Budker, D., Kitching, J., Schwindt, P.D.D., and Stalnaker, J.E. (2006). Magnetometry with millimeter-scale anti-relaxation-coated alkali-metal vapor cells. *Journal of the Optical Society of America B. 23* (6), 1001–1006, DOI:10.1364/JOSAB.23.001001.
7. Sarkisyan, D., Bloch, D., Papoyan, A., and Ducloy, M. (2001). Sub-Doppler spectroscopy by sub-micron thin Cs vapor layer. *Opt. Commun. 200, 201,* DOI: 10.1016/S0030-4018(01)01604-2.

8. Hakhumyan, G.T. (2012). Optical magnetometer with submicron spatial resolution based on Rb vapors. *Journal of Contemporary Physics*. *47* (3), 105–112, DOI: 10.3103/S1068337212030024.
9. Blushs, K., and Auzinsh, M. (2004). Validity of rate equations for Zeeman coherences for analysis of nonlinear interaction of atoms with broadband laser radiation. *Phys. Rev. A*, *69*, 063806, DOI:10.1103/PhysRevA.69.063806.
10. Auzinsh, M., Ferber, R., Gahbauer, F., Jarmola, A., and Kalvans, L. (2008). F-resolved magneto-optical resonances in the D1 excitation of caesium: Experiment and theory. *Phys. Rev. A*, *78*, 013417, DOI: 10.1103/PhysRevA.78.013417.
11. Auzinsh, M., Ferber, R., Gahbauer, F., Jarmola, A., and Kalvans, L. (2009). Nonlinear magneto-optical resonances at D1 excitation of 85Rb and 87Rb for partially resolved hyperfine F levels. *Phys. Rev. A*, *79*, 053404, DOI: 10.1103/PhysRevA.79.053404.
12. Auzinsh, M., Berzins, A., Ferber, R., Gahbauer, F., Kalvans, L., Mozers, A., and Opalevs, D. (2012). Conversion of bright magneto-optical resonances into dark resonances at fixed laser frequency for D2 excitation of atomic rubidium. *Phys. Rev. A*, *85*, 033418, DOI:10.1103/PhysRevA.85.033418.
13. Auzinsh, M., Ferber, R., Gahbauer, F., Jarmola, A., Kalvans, L., Papoyan, A., and Sarkisyan, D. (2010). Nonlinear magneto-optical resonances at D1 excitation of 85Rb and 87Rb in an extremely thin cell. *Phys. Rev. A*, *81*, 033408, DOI:10.1103/PhysRevA.81.033408.

MAGNĒTISKĀ LAUKA GRADIOMETRS AR TELPISKO IZŠĶIRTSPĒJU ZEM MIKROMETRA, KURA DARBĪBAS PAMATĀ IR CĒZIJA TVAIKI ĻOTI PLĀNAJĀ ŠŪNĀ

M. Auziņš, A. Bērziņš, R. Ferbers, F. Gahbauers, U. Kalniņš,
R. Rundāns, D. Sarkisyan

Kopsavilkums

Šajā darbā mēs aprakstam iekārtu magnētiskā lauka un tā gradienta mērīšanai ar dažu simtu nanometru telpisko izšķirtspēju. Šīs iekārtas darbības pamatā ir cēzija metāla tvaiki, kas atrodas ļoti plānajā šūnā. Tika mērīts absorbcijas signāls, un izmantotā lāzera jauda bija ļoti zema, kas savukārt varētu būt interesanti modernām ražošanas metodēm. Pētījuma rezultātā tika izveidota portatīva un pilnīgi automatizēta iekārta.

08.04.2015.

Spatial dynamics of laser-induced fluorescence in an intense laser beam: experiment and theory in alkali metal atoms

M. Auzinsh,* A. Berzins, R. Ferber, F. Gahbauer, and U. Kalnins
Laser Centre, The University of Latvia, 19 Rainis Boulevard, LV-1586 Riga, Latvia

(Dated: January 26, 2016)

We show that it is possible to model accurately optical phenomena in intense laser fields by taking into account the intensity distribution over the laser beam. We present an extension of an earlier theoretical model that divides an intense laser beam into concentric regions, each with a Rabi frequency that corresponds to the intensity in that region, and solve a set of coupled optical Bloch equations for the density matrix in each region. Experimentally obtained magneto-optical resonance curves for the $F_g = 2 \longrightarrow F_e = 1$ transition of the D_1 line of ^{87}Rb agree very well with the theoretical model up to a laser intensity of around 200 mW/cm^2 for a transition whose saturation intensity is around 4.5 mW/cm^2. We examine the spatial dependence of the fluorescence intensity in an intense laser beam experimentally and theoretically. We present and discuss the results of an experiment in which a broad, intense pump laser excites the $F_g = 4 \longrightarrow F_e = 3$ transition of the D_2 line of Cesium while a narrow probe beam scans the atoms within the pump beam and excites the D_1 line of Cesium, whose fluorescence is recorded as a function of probe beam position. Experimentally obtained spatial profiles of the fluorescence intensity agree qualitatively with the predictions of the model.

PACS numbers: 32.60.+i,32.80.Xx,32.10.Fn

I. INTRODUCTION

Coherent radiation can polarize the angular momentum distribution of an ensemble of atoms in various ways, creating different polarization moments, which modify the way these atoms will interact with radiation. Carefully prepared spin polarized atoms can make the absorption highly dependent on frequency (electromagnetically induced transparency [1]), causing large values of the dispersion, which, in turn, are useful for such interesting effects as slow light [2] and optical information storage [3]. Electric and magnetic fields, external or inherent in the radiation fields, may also influence the time evolution of the spin polarization and cause measurable changes in absorption or fluorescence intensity and/or polarization. These effects are the basis of many magnetometry schemes [4, 5], and must be taken into account in atomic clocks [6] and when searching for fundamental symmetry violations [7] or exotic physics such as an electric dipole moment of the electron [8]. Sufficiently strong laser radiation creates atomic coherences in the excited as well as in the ground state [9] The coherences are destroyed when the Zeeman sublevel degeneracy is removed by a magnetic field. Since the ground state has a much longer lifetime, very narrow magneto-optical resonances can be created, which are related to the ground-state Hanle effect (see [10] for a review). Such resonances were first observed in cadmium in 1964 [11].

The formation of dark magneto-optical resonances has been understood for some time (see [7, 9, 12] for a review), and bright (opposite sign) magneto-optical resonances have also been observed and explained [13–15]; the challenge in describing experiments lies in choosing the effects to be included in the numerical calculations so as to find a balance between computation time and accuracy. The optical Bloch equations (OBEs) for the density matrix have been used as early as 1978 to model magneto-optical resonances [16]. In order to achieve greater accuracy, later efforts to model signals took into account effects such as Doppler broadening, the coherent properties of the laser radiation, and the mixing of magnetic sublevels in an external magnetic field to produce more and more accurate descriptions of experimental signals [17]. Analytical models can also achieve excellent descriptions of experimental signals under weak excitation, i.e., in the lowest nonlinear order of laser power [18, 19]. In recent years, excellent agreement has been achieved by numerical calculations even when optical pumping plays a role. However, as soon as the laser radiation begins to saturate the absorption transition, the model's accuracy suffers. The explanation has been that at high radiation intensities, it is no longer possible to model the relaxation of atoms moving in and out of the beam with a single rate constant [17, 20]. Nevertheless, accurate numerical models of magneto-optical effects in an intense laser field are very desirable, because they could arise in a number of experimental situations[18, 19, 21–24]. Therefore, we have set out to model magneto-optical effects in the presence of intense laser radiation by taking into account the fact that an atom experiences different laser intensity values as it passes through a beam. In practice, we solve the rate equations for the Zeeman coherences for different regions of the laser beam with a value of the Rabi frequency that more closely approximates the real situation in that part of the beam. To save computing time, stationary solutions to the rate equa-

---

*Electronic address: `Marcis.Auzins@lu.lv`

tions for Zeeman sublevels and coherences are sought for each region [25]. With this simplification, and by taking into account the motion of atoms through the beam, we can now obtain accurate descriptions of experimental signals up to much higher intensities while maintaining reasonable computing times. Moreover, the model can be used to study the spatial distribution of the laser induced fluorescence within the laser beam. We report here the results of a theoretical and experimental study that involves two overlapping lasers: one spatially broad, intense pump laser, and a weaker, tightly focused, spatially narrow probe laser. The qualitative agreement between experimental and theoretical fluorescence intensity profiles indicates that the model is a useful tool for studying fluorescence dynamics as well as for modelling magneto-optical signals at high laser intensities.

II. THEORY

The theoretical model used here is a further development of previous efforts [26], which has been subjected to some initial testing in the specialized context of an extremely thin cell [24]. The description of coherent processes starts with the OBE:

$$i\hbar\frac{\partial\rho}{\partial t} = \left[\hat{H},\rho\right] + i\hbar\hat{R}\rho, \tag{1}$$

where ρ is the density matrix describing the atomic state, $\hat{H}$ is the Hamiltonian of the system, and $\hat{R}$ is an operator that describes relaxation. These equations are transformed into rate equations that are solved under stationary conditions in order to obtain the Zeeman coherences in the ground ($\rho_{g_i g_j}$) and excited ($\rho_{e_i e_j}$) states [25]. However, when the intensity distribution in the beam is not homogeneous, more accurate results can be achieved by dividing the laser beam into concentric regions and solving the OBEs for each region separately, while accounting for atoms that move into and out of each region as they fly through the beam. Figure 1 illustrates the idea. The top part of the figure shows the intensity profile of the laser beam, while the bottom part of the figure shows a cross-section of the laser beam indicating the concentric regions.

In order to account for particles that leave one region and enter the next, an extra term must be added to the OBE:

$$-i\hbar\hat{\gamma}_t\rho + i\hbar\hat{\gamma}_t\rho'. \tag{2}$$

In this term, ρ' is the density matrix of the particles entering the region with index $n+1$ (identical to the density matrix of the particles leaving the previous region), and $\hat{\gamma}_t$ is an operator that accounts for transit relaxation. This operator is essentially a diagonal matrix with elements $\hat{\gamma}_{t_{ij}} = ({}^{v_{yz}}/_{s_n})\delta_{ij}$, where v_{yz} characterizes the particle speed in the plane perpendicular to the beam and s_n is the linear dimension of the region. To simplify matters, we treat particle motion in only one direction and later average with particles that move in the other direction. In that case, $\rho' = \rho^{n-1}$. Thus, the rate equations for the density matrix ρ^n of the n^{th} region become

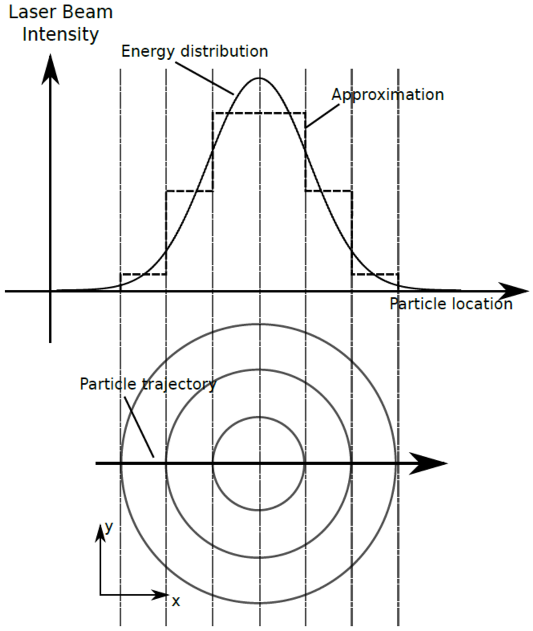

FIG. 1: Laser beam profile split into a number of concentric regions.

$$\begin{aligned} i\ \hbar\frac{\partial\rho^n}{\partial t} &= \left[\hat{H},\rho^n\right] + i\ \hbar\hat{R}\rho^n - i\ \hbar\hat{\gamma_t}^n\rho^n \\ &+ i\ \hbar\hat{\gamma_t}^n\rho^{n-1} - i\ \hbar\hat{\gamma}_c\rho^n + i\ \hbar\hat{\gamma}_c\rho^0. \end{aligned} \tag{3}$$

In this equation the relaxation operator $\hat{R}$ describes spontaneous relaxation only and $\hat{\gamma}_c$ is the collisional relaxation rate, which, however, becomes significant only at higher gas densities.

Next, the rotating wave approximation [27] is applied to the OBEs, which yield stochastic differential equations that can be simplified by means of the decorrelation approach [28]. Since the measurable quantity is merely light intensity, a formal statistical average is performed over the fluctuating phases of these stochastic equations, making use of the decorrelation approximation [25]. As a result, the density matrix elements that correspond to optical coherences are eliminated and one is left with rate equations for the Zeeman coherences:

$$\begin{aligned}
\frac{\partial \rho^n_{g_i,g_j}}{\partial t} = & \sum_{e_k,e_m} \left(\Xi^n_{g_ie_m} + (\Xi^n_{e_kg_j})^*\right) d^*_{g_ie_k} d_{e_mg_j} \rho^n_{e_ke_m} \\
& - \sum_{e_k,g_m} (\Xi^n_{e_kg_j})^* d^*_{g_ie_k} d_{e_kg_m} \rho^n_{g_mg_j} \\
& - \sum_{e_k,g_m} \Xi^n_{g_ie_k} d^*_{g_me_k} d_{e_kg_j} \rho^n_{g_ig_m} \\
& - i\omega_{g_ig_j} \rho^n_{g_ig_j} + \sum_{e_ke_l} \Gamma^{e_ke_l}_{g_ig_j} \rho^n_{e_ke_l} - \gamma_t \rho^n_{g_ig_j} \\
& + \gamma^n_t \rho^{n-1}_{g_ig_j} - \gamma^n_c \rho^n_{g_ig_j} + \gamma_c \rho^0_{g_ig_j}
\end{aligned} \tag{4}$$

$$\begin{aligned}
\frac{\partial \rho^n_{e_i,e_j}}{\partial t} = & \sum_{g_k,g_m} \left((\Xi^n_{e_ig_m})^* + \Xi^n_{g_ke_j}\right) d^*_{e_ig_k} d_{g_me_j} \rho^n_{g_kg_m} \\
& - \sum_{g_k,e_m} \Xi^n_{g_ke_j} d_{e_ig_k} d^*_{g_ke_m} \rho^n_{e_me_j} \\
& - \sum_{g_k,e_m} (\Xi^n_{e_ig_k})^* d_{e_mg_k} d^*_{g_ke_j} \rho^n_{e_ie_m} \\
& - i\omega_{e_ie_j} \rho^n_{e_ie_j} - \Gamma \rho^n_{e_ie_j} - \gamma^n_t \rho^n_{e_ie_j} \\
& + \gamma^n_t \rho^{n-1}_{e_ie_j} - \gamma_c \rho^n_{e_ie_j}.
\end{aligned} \tag{5}$$

In both equations, the first term describes the population increase and the creation of coherence as a result of induced transitions, the second and third terms describe population loss due to induced transitions, the fourth term describes the destruction of Zeeman coherences due to the respective splitting $\omega_{g_ig_j}$ or $\omega_{e_ie_j}$ of the Zeeman sublevels in an external magnetic field. The fifth term in Eq. 5 describes spontaneous decay with $\Gamma\rho^n_{e_ie_j}$ giving the spontaneous rate of decay for the excited state. At the same time the fifth term in Eq. 4 describes the transfer of population and coherences from the excited-state matrix element $\rho_{e_ke_l}$ to the ground-state density matrix element $\rho_{g_ig_j}$ with rate $\Gamma^{e_ke_l}_{g_ig_j}$. These transfer rates are related to the rate of spontaneous decay Γ for the excited state. Explicit expressions for these $\Gamma^{e_ke_i}_{g_ig_j}$ can be calculated from quantum angular momentum theory and are given in [9]. The remaining terms have been described previously in the context of Eqns. 2 and 3. The laser beam interaction is represented by the term

$$\Xi_{g_ie_j} = \frac{|\boldsymbol{\varepsilon}^n|^2}{\frac{\Gamma+\Delta\omega}{2} + i\left(\bar{\omega} - \mathbf{k}\cdot\mathbf{v} + \omega_{g_ie_j}\right)}, \tag{6}$$

where $|\boldsymbol{\varepsilon}^n|^2$ is the laser field's electric field strength in the nth region, Γ is the spontaneous decay rate, $\Delta\omega$ is the laser beam's spectral width, $\bar{\omega}$ is the laser frequency, $k \cdot v$ gives the Doppler shift, and $\omega_{g_ie_j}$ is the difference in energy between levels g_i and e_j. The system of linear equations can be solved for stationary conditions to obtain the density matrix ρ.

From the density matrix one can obtain the fluorescence intensity from each region for each velocity group v and given polarization $\boldsymbol{\varepsilon}_f$ up to a constant factor of $\tilde{I}_0$ [29–31]:

$$I_n(v, \boldsymbol{\varepsilon}_f) = \tilde{I}_0 \sum_{g_i,e_j,e_k} d^{*(ob)}_{g_ie_j} d^{(ob)}_{e_kg_i} \rho_{e_je_k}. \tag{7}$$

From these quantities one can calculate the total fluorescence intensity for a given polarization $\boldsymbol{\varepsilon}_f$:

$$I(\boldsymbol{\varepsilon}_f) = \sum_n \sum_v f(v)\Delta v \frac{A_n}{A} I_n(v, \boldsymbol{\varepsilon}_f). \tag{8}$$

Here the sum over n represents the sum over the different beam regions of relative area ${}^{A_n}/_{A}$ as they are traversed by the particle, v is the particle velocity along the laser beam, and $f(v)\Delta v$ gives the number of atoms with velocity $v \pm {}^{\Delta v}/_{2}$.

In practice, we do not measure the electric field strength of the laser field, but the intensity $I = P/A$, where P is the laser power and A is the cross-sectional area of the beam. In the theoretical model it is more convenient to use the Rabi frequency Ω_R, here defined as follows:

$$\Omega_R = k_R \frac{||d|| \cdot ||\epsilon||}{\hbar} = k_R \frac{||d||}{\hbar} \sqrt{\frac{2I}{\epsilon_0 n c}}, \tag{9}$$

where $||d||$ is the reduced dipole matrix element for the transition in question, ϵ_0 is the vacuum permittivity, n is the index of refraction of the medium, c is the speed of light, and k_R is a factor that would be unity in an ideal case, but is adjusted to achieve the best fit between theory and experiment since the experimental situation will always deviate from the ideal case in some way. We assume that the laser beam's intensity distribution follows a Gaussian distribution. We define the average value of Ω_R for the whole beam by taking the weighted average of a Gaussian distribution in the interval [0,FWHM/2], where FWHM is the full width at half maximum. Thus it follows that the Rabi frequency at the peak of the intensity distribution (see Fig. 1) is $\Omega_R = 0.721\Omega_{peak}$. From there the Rabi frequency of each region can be obtained by scaling by the value of the Gaussian distribution function.

When modeling two beams (as in Sec. V), the multiregion approach is applied to each beam in a manner shown in Fig. 2. The wide beam is referred to as the pump beam, whereas the narrow beam is referred to as the probe beam. In this case, pump and probe refer to the beam diameter, which is related to their function in the experiment, rather than to the beam intensity. The reason is that the probe beam's function is to explore the population distribution of atoms inside the wider pump beam. It should be noted, that the probe intensity in the outer regions of the pump beam can significantly exceed the pump beam intensity. Additionally the probe beam is always considered to be located inside one of the pump beam regions, and the width of the probe beam roughly coincides with the width of the pump beam region (see Fig. 2).

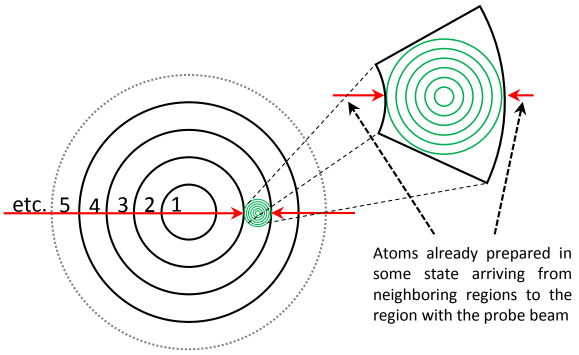

FIG. 2: (Color online) Illustration of the way the theoretical calculations treat the pump beam (wide concentric rings) and the probe beam (a set of smaller rings in the 3rd region of the pump beam). The atoms entering the region with the probe beam, have crossed multiple pump beam regions, thus they are already prepared in some state.

At first, Eq. (3) is used to calculate the density matrix that results from the interaction of the pump beam with the atoms while the probe beam is ignored. In the next step, the probe beam is divided into regions out to 3 standard deviations (assuming a Gaussian probe beam). The pump intensity is taken to be constant over the probe beam, which means that the density matrix from the neighboring pump regions can be used to calculate the atoms entering the probe beam from either side. The Hamiltonian and relaxation terms in Eq. (3) are now supplemented to include interactions with both probe and pump beam, and the system is solved for the regions of the probe beam in the presence of a pump field of constant intensity. For that purpose the index n in (3) is replaced with (n, m), and, following the same inference, one obtains equations for the description of two laser fields.

In the theoretical calculations the only observation direction is along the quantization axis.

III. EXPERIMENTAL SETUP

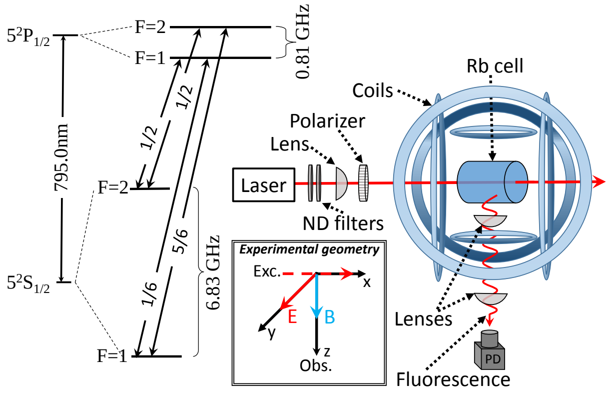

FIG. 3: (Color online) Basic experimental setup for measuring magneto-optical resonances. The inset on the left shows the level diagram of ^{87}Rb [33]. The other inset shows the geometrical orientation of the electric field vector E, the magnetic field vector B, and laser propagation direction (Exc.) and observation direction (Obs.).

The theoretical model is tested with two experiments. The first experiment measures magneto-optical resonances on the D_1 line of ^{87}Rb and is shown schematically in Fig. 3. The experiment has been described elsewhere along with a comparison to an earlier version of the theoretical model that did not divide the laser beam into separate regions [32]. The laser used in the experiment is an extended cavity diode laser, whose frequency can be scanned by applying a voltage to a piezo crystal attached to the grating. Neutral density (ND) filters are used to regulate the laser intensity, and linear polarization is obtained using a Glan-Thomson polarizer. A set of three orthogonal Helmholtz coils scans the magnetic field along the z axis while compensating the ambient field in the other directions. The Helmholtz coils also provide a homogeneous magnetic field inside the cell. The innermost coil had a diameter of 187.5 mm and consisted of 225 turns of 1.5 mm diameter copper wire. A pyrex cell with a natural isotopic mixture of Rubidium at room temperature is located at the center of the coils. The total laser induced fluorescence (LIF) in a selected direction (without frequency or polarization selection) is detected with a photodiode (Thorlabs FDS-100 with active area of 13 mm^2) and data are acquired with a data acquisition card (National Instruments 6024E, A/D Converter resolution: 12 bit, data rate: 50 kS/s) or a digital oscilloscope (Agilent DSO5014, A/D Converter resolution: 8 bit, data rate: 2.5 kS/s). To generate the magnetic field scan with a rate of about 1 Hz, a computer-controlled analog signal is applied to a bipolar power supply (Kepco BOP-50-8M). In the measurements we used up to 1A, and the current stability was estimated to be around 0.5% of the rating. The laser frequency is simultaneously scanned at a rate of about 10-20 MHz/s, and is measured by a wavemeter (HighFinesse WS-7). The laser beam is characterized using a beam profiler (Thorlabs BP104-VIS).

A second experimental setup is used to study the spatial profile of the fluorescence generated by atoms in a laser beam at resonance. It is shown in Fig. 4. Here two lasers are used to excite the D_1 and D_2 transitions of Cesium. Both lasers are based on distributed feedback diodes from Toptica (DL100-DFB, both tunable in 25 GHz frequency range). One of the lasers (Cs D_2) serves as a pump laser with a spatially broad and intense beam, while the other (Cs D_1), spatially narrower beam probes the fluorescence dynamics within the pump beam. Figure 5 shows the level scheme of the excited transitions. Both lasers are stabilized with saturation absorption signals from cells shielded by three layers of mu-metal. Mu-metal shields are used to avoid frequency drifts due to

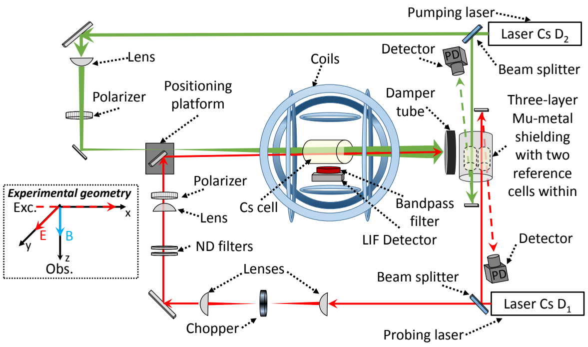

FIG. 4: (Color online) Experimental setup for the two-laser experiment. The lasers are stabilized by two Toptica Digilok modules locked to error signals generated from saturated absorption spectroscopy measurements made in a separate, magnetically shielded cells.

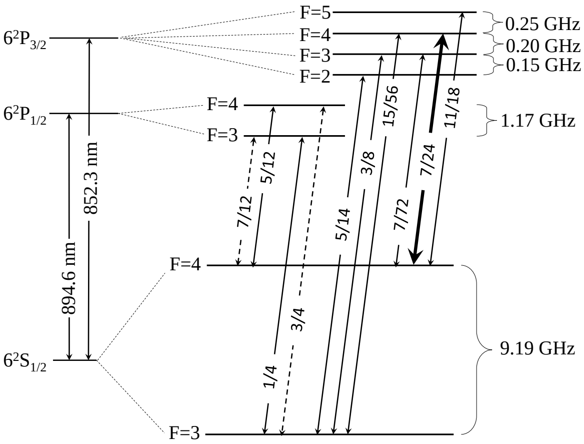

FIG. 5: Level scheme for the two-laser experiment. The bold, solid arrow represents the pump laser transition, whereas the arrows with dashed lines represent the scanning laser transitions. Other transitions are given as thin, solid lines.

the magnetic field scan performed in the experiment and other magnetic field fluctuations in the laboratory.

To reduce the amount of scattered light entering the detector, the Cesium cell is wrapped in black paper with a small opening (5 mm ×2 mm) for fluorescence measurements. A bandpass filter (890 nm ± 10 nm) is placed before the photodiode. To reduce noise from the intense pump beam, the probe beam is modulated by placing a mechanical chopper (providing a 2.4 kHz chopping frequency) near its focus, and the fluorescence signal passes through a lock-in amplifier and is recorded on a digital oscilloscope (Yokogawa DL-6154, A/D Converter resolution: 8 bit, data rate: 2.5 kS/s). The probe laser is scanned through the pump laser beam profile using a mirror mounted on a moving platform (Nanomax MAX301 from Thorlabs) with a scan range of 8 mm in one dimension. The probing beam itself has a FWHM diameter of 200 µm with typical laser power of 100 µW. The pump beam width is 1.3 mm (FWHM) and its power is 40 mW. This laser beam diameter is achieved by letting the laser beam slowly diverge after passing the focal point of a lens with focal length of 1 m. The pump laser beam diverges slowly enough so that the beam diameter within the vapor cell is effectively constant. The probe beam is also focused by an identical lens to reach its focus point inside the cell.

In both experiments described in this section, the estimated solid angle of fluorescence observation is around 0.02 sr.

IV. APPLICATION OF THE MODEL TO MAGNETO-OPTICAL SIGNALS OBTAINED FOR HIGH LASER POWER DENSITIES

For a first test for the numerical model with multiple regions inside the laser beam, we use the model to calculate the shapes of magneto-optical resonances for ^{87}Rb in an optical cell. The experimental setup has been described earlier (see Fig. 3). Figure 6(a)–(c) show experimental signals (dots) and theoretical calculations (curves) of magneto-optical signals in the $F_g = 2 \longrightarrow F_e = 1$ transition of the D_1 line of ^{87}Rb. Three theoretical curves are shown: curve N1 is calculated assuming a laser beam with a single average intensity; curve N20 is calculated using a laser beam divided into 20 concentric regions of equal width, and assuming that all the particles traverse the laser beam crossing its center; curve N20MT is calculated in the same way as curve N20, but furthermore the results were averaged also over trajectories that did not pass through the center, i.e., taking into account the particles that skim the Gaussian laser beam profile wings. As the model starts to converge rapidly with only ten regions and with diminishing returns for using additional regions, we choose twenty regions because the computational cost is reasonable and the accuracy is more than sufficient even at the highest laser power densities. At the relatively low Rabi frequency of $\Omega_R = 2.5$ MHz [Fig. 6(a)] all calculated curves practically coincide and describe well the experimental signals. The single region model treats the beam as a cylindrical beam with an intensity of 2 mW/cm^2, which is below the saturation intensity for that transition of 4.5 mW/cm^2 [33]. When the laser intensity is 20 mW/cm^2 ($\Omega_R = 8.0$ MHz), well above the saturation intensity, model N1 is no longer adequate for describing the experimental signals and model N20MT works slightly better [Fig. 6(b)]. In particular, the resonance becomes sharper and sharper as the intensity increases, and models N20 and N20MT reproduce this sharpness. Even at an intensity around 200 mW/cm^2 ($\Omega_R = 25$ MHz), the models with 20 regions describe the shape of the experimental curve quite well, while model N1 describes the experimental results poorly in terms of width and overall shape [Fig. 6(c)].

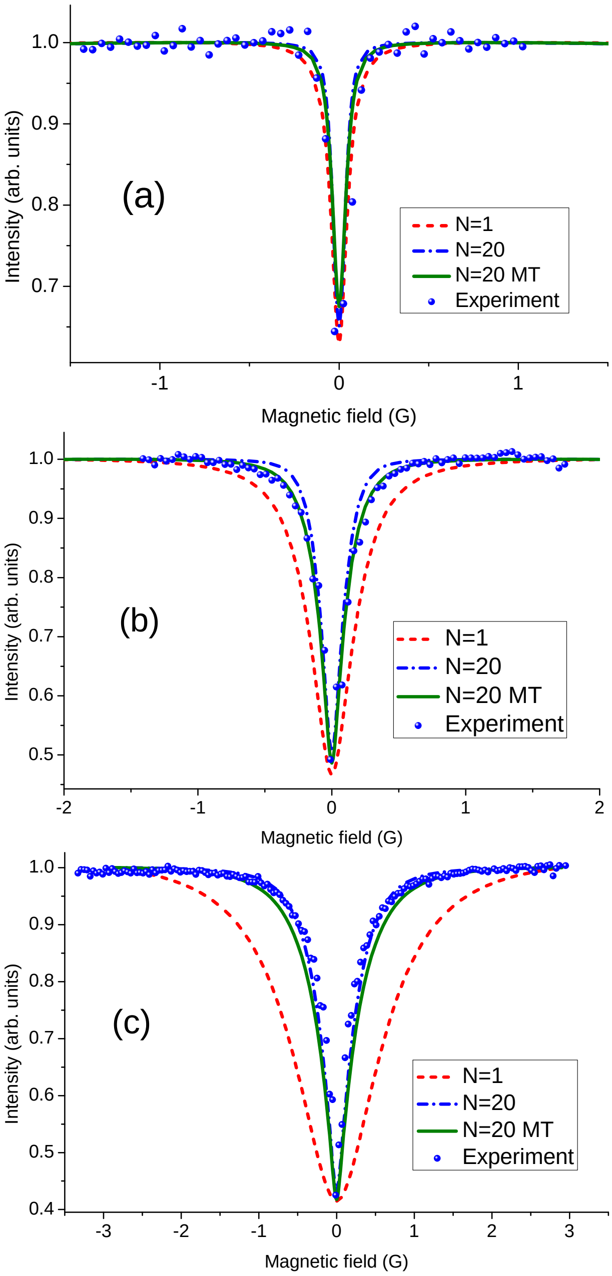

FIG. 6: (Color online) Magneto-optical resonances for the $F_g = 2 \longrightarrow F_e = 1$ transition of the D_1 line of ^{87}Rb. Filled circles represent experimental measurements for (a) 28 μW (Ω_R=2.5 MHz) (b) 280 μW (Ω_R=8.0 MHz), and (c) 2800 μW (Ω_R=25 MHz). Curve N1 (dashed) shows the results of a theoretical model that uses one Rabi frequency to model the entire beam profile. Curve N20 (dash-dotted) shows the result of the calculation when the laser beam profile is divided into 20 concentric rings, and the optical Bloch equations are solved separately for each ring. Curve N20MT (solid) shows the results for a calculation with 20 concentric regions when trajectories are taken into account that do not pass through the center of the beam.

V. INVESTIGATION OF THE SPATIAL DISTRIBUTION OF FLUORESCENCE IN AN INTENSE LASER BEAM

A. Theoretical investigation of the spatial dynamics of fluorescence in an extended beam

In order to describe the magneto-optical signals in the previous sections, the fluorescence from all concentric beam regions in models N20 and N20MT is summed, since usually experiments measure only total fluorescence (or absorption), especially if the beams are narrow. However, solving the optical Bloch equations separately for different concentric regions of the laser beam, it is possible to calculate the strength of the fluorescence as a function of distance from the center of the beam. With an appropriate experimental technique, the distribution of fluorescence within a laser beam can also be measured.

Figure 7 shows the calculated fluorescence distribution as a function of position in the laser beam. As atoms move through the beam in one direction, the intense laser radiation optically pumps the ground state. In a very intense beam, the ground state levels that can absorb light have been emptied while traversing the outer regions, and thus the central regions will less intense fluorescence (solid, green curve). Since atoms are actually traversing the beam from all directions, the result is a fluorescence profile with a reduced intensity in the central regions of the beam (dashed, red curve). The effect of increasing the laser beam intensity (or Rabi frequency) can be seen in Fig. 8. At a Rabi frequency of $\Omega_R = 0.6$ MHz, the fluorescence profile tracks the intensity profile of the laser beam exactly. When the Rabi frequency is increased ten times ($\Omega_R = 6.0$ MHz), which corresponds to an intensity increase of 100, the fluorescence profile already

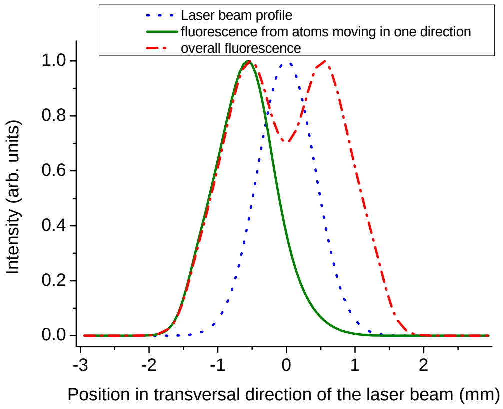

FIG. 7: (Color online) Theoretical simulation of fluorescence distribution in an intense laser beam, where zero marks the center of the laser beam. Dotted (blue) line—laser beam profile, solid (green) line—fluorescence from atoms moving in one direction; dash-dotted (red) line—the overall fluorescence as a function of position that results from averaging all beam trajectories.

appears somewhat deformed and wider than the actual laser beam profile. At Rabi frequencies of $\Omega_R = 48.0$ MHz and greater, the fluorescence intensity at the center of the intense laser beam is weaker than towards the edges as a result of the ground state being depleted by the intense radiation before the atoms reach the center of the laser beam. If one were to excite a dark state using an intense beam with a much larger radius, the resulting fluorescence distribution would be expected to look like an intense (narrow) ring at the border of the of the laser beam, and the inner regions would exhibit a flat, less intense structure. If one were to excite a bright state with such a beam, one would expect a roughly Gaussian fluorescence distribution with a flattened top.

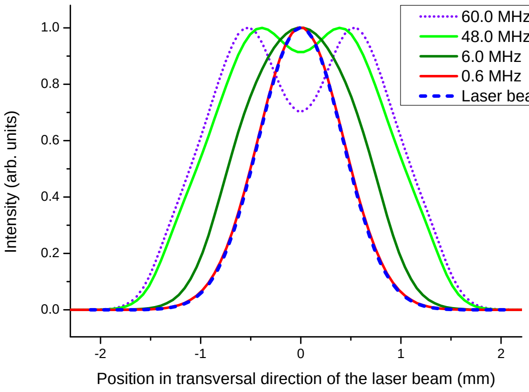

FIG. 8: (Color online) Calculated fluorescence distribution as a function of position in the laser beam for various values of the Rabi frequency. As the Rabi frequency increases, the distribution becomes broader.

B. Experimental study of the spatial dynamics of excitation and fluorescence in an intense, extended beam

In order to test our theoretical model of the spatial distribution of fluorescence from atoms in an intense, extended pumping beam, we record magneto-optical resonances from various positions in the pumping beam. As the probe beam used in this experiment is relatively strong, the multiple region approach is also applied to it, and in the calculations the probe beam is divided into six regions (see Fig. 2 and the accompanying description in Sec. II for details on the treatment of two beams). It has to be pointed out that the experiment with the two laser beams is performed in order to cross-check the theoretical model with the multiple region approach, and the coincidence between calculations and the experiment is expected to be qualitative. Thus, there are some approximations done to make the calculation times reasonable. In particular, by two stages of the calculations described in Sec. II, we assume that the probe beam does not contribute to the preparation of atoms that fly into the region with the two beams (pump and probe). Besides that, only trajectories crossing the center of the pump beam are taken into account, and the width of the probe beam is considered to coincide with the width of a pump beam region.

The experimental setup is shown in Fig. 4. To visualize these data, surface plots are generated where one horizontal axis represents the magnetic field and the other, the position of the probe beam relative to the pump beam axis. The height of the surface represents the fluorescence intensity. In essence, the surface consists of a series of magneto-optical resonances recorded for a series of positions of the probe beam axis relative the the pump beam axis. Figure 9 shows the results for experiments (a) and calculations (b) for the pump beam tuned to the $F_g = 4 \longrightarrow F_e = 4$ transition of the Cs D_2 line and the probe beam tuned to the $F_g = 4 \longrightarrow F_e = 3$ transition of the Cs D_1 line. One can see that the theoretical plot reproduces qualitatively all the features of the experimental measurement. Similar agreement can be observed when the probe beam is tuned to the $F_g = 3 \longrightarrow F_e = 4$ transition of the Cs D_1 line, as shown in Fig. 10.

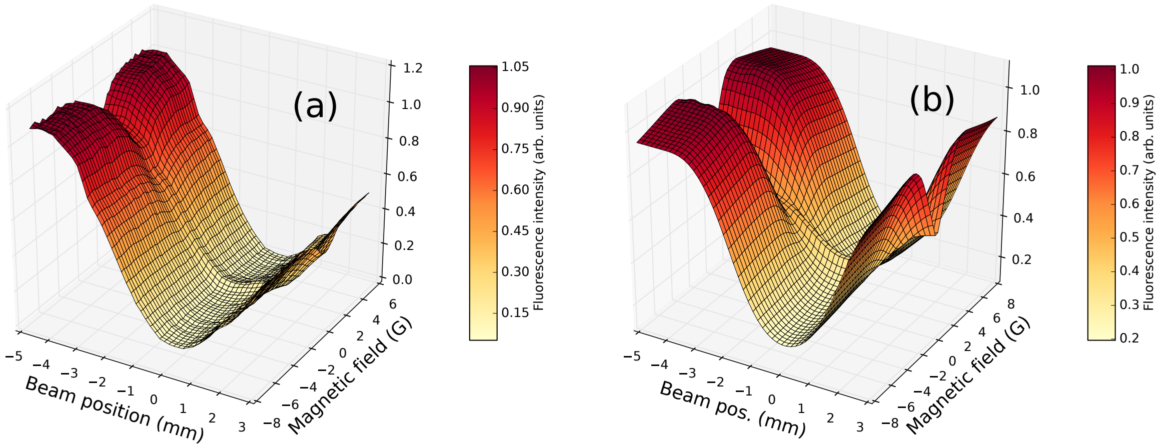

FIG. 9: (Color online) Magneto-optical resonances produced for various positions of the probing laser beam ($F_g = 4 \longrightarrow F_e = 3$ transition of the D_1 line of Cesium) with respect to the pump laser beam ($F_g = 4 \longrightarrow F_e = 4$ transition of the D_2 line of Cesium): (a) experimental results and (b) theoretical calculations.

VI. CONCLUSIONS

We show how to model magneto-optical signals more accurately at laser intensities significantly higher than the saturation intensity by dividing the laser beam into concentric circular regions and solving the rate equations for Zeeman coherences in each region while taking into account the actual laser intensity in that region and the transport of atoms between regions. We discuss results of using this approach for modeling magneto-optical resonances for the $F_g = 2 \longrightarrow F_e = 1$ transitions of the D_1 line of ^{87}Rb, comparing the calculated curves to measured signals. We demonstrate that good agreement between theory and experiment can be achieved up to Rabi frequencies of at least 25 MHz, which corresponds to a laser intensity of 200 mW/cm^2, or more than 40 times the saturation intensity of the transition. As an additional check on the model, we present results from a theoretical and experimental study of the spatial distribution of the fluorescence intensity within a laser beam. The results indicated that at high laser power densities, the maximum fluorescence intensity is not produced in the center of the beam, because the atoms have been pumped free of absorbing levels prior to reaching the center. We compare experimental and theoretical signals of magneto-optical resonance signals obtained by exciting Cesium atoms with a narrow probe beam tuned to the D_1 transition at various locations inside a region illuminated by an intense pump beam tuned to the D_2 transition and obtain good qualitative agreement.

Acknowledgments

We gratefully acknowledge support from the Latvian Science Council Grant Nr. 119/2012 and from the University of Latvia Academic Development Project Nr. AAP2015/B013.

---

[1] S. E. Harris, J. E. Field, and A. Imamoglu, Physical Review Letters **64**, 1107 (1990).

[2] L. V. Hau, S. E. Harris, Z. Dutton, and C. H. Behroozi, Nature **397**, 594 (1999).

[3] C. Liu, Z. Dutton, C. H. Behroozi, and L. V. Hau, Nature **409**, 490 (2001).

[4] M. O. Scully and M. Fleischhauer, Phys. Rev. Lett. **69**, 1360 (1992).

[5] D. Budker and M. V. Romalis, Nature Physics **3**, 227 (2007).

[6] S. Knappe, P. D. D. Schwindt, V. Shah, L. Hollberg, J. Kitching, L. Liew, and J. Moreland, Opt. Express **13**, 1249 (2005).

[7] D. Budker, W. Gawlik, D. F. Kimball, S. M. Rochester, V. V. Yashchuk, and A. Weis, Reviews of Modern Physics **74**, 1153 (2002), ISSN 15390756.

[8] B. Regan, E. D. Commins, C. J. Schmidt, and D. DeMille, Phys. Rev. Lett. **88**, 071805 (2002), URL `http://journals.aps.org/prl/abstract/10.1103/PhysRevLett.88.071805`.

[9] M. Auzinsh, D. Budker, and S. M. Rochester, *Optically Polarized Atoms* (Oxford University Press, Great Cardendon Street, 2010), ISBN 978-0-19-956512-2.

[10] E. Arimondo (Elsevier, 1996), vol. 35 of *Elsevier Science B.V.*, p. 259, ISBN 978-0-444-82309-0.

[11] J. C. Lehmann and C. Cohen-Tannoudji, C.R. Acad. Sci. (Paris) **258**, 4463 (1964).

[12] E. B. Alexandrov, M. Auzinsh, D. Budker, D. F. Kimball, S. Rochester, and V. V. Yashchuk, J. Opt. Soc. Am. B **22**, 7 (2005).

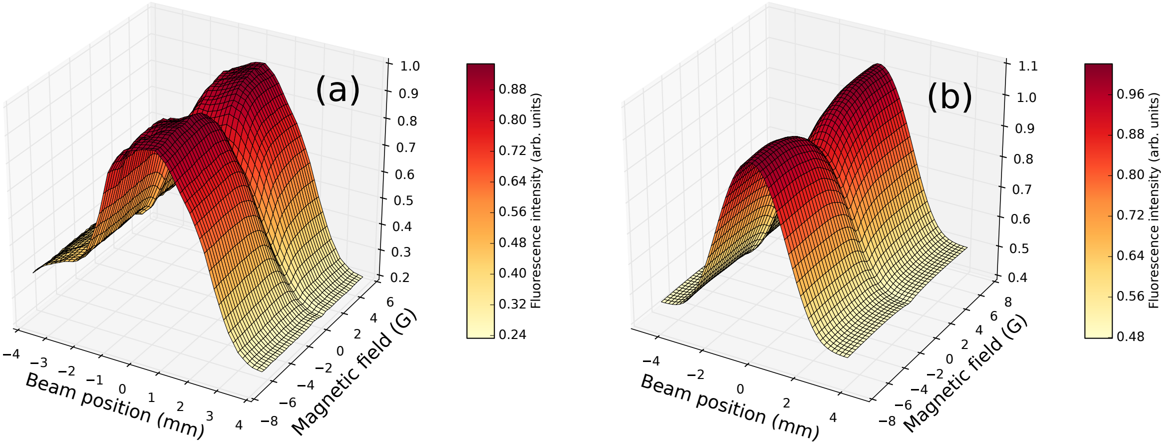

FIG. 10: (Color online) Magneto-optical resonances produced for various positions of the probe laser beam ($F_g = 3 \longrightarrow F_e = 4$ transition of the D_1 line of Cesium) with respect to the pump laser beam ($F_g = 4 \longrightarrow F_e = 4$ transition of the D_2 line of Cesium): (a) experimental results and (b) theoretical calculations.

[13] A. P. Kazantsev, V. S. Smirnov, A. M. Tumaikin, and I. A. Yagofarov, Opt. Spectrosk. (USSR) **57**, 116 (1984).

[14] F. Renzoni, S. Cartaleva, G. Alzetta, and E. Arimondo, Physical Review A **63**, 065401 (2001).

[15] J. Alnis and M. Auzinsh, Physical Review A **63**, 023407 (2001), arXiv:physics/0011050.

[16] J. L. Picqué, J. Phys. B: Atom. Molec. Phys. **11**, L59 (1978).

[17] M. Auzinsh, R. Ferber, F. Gahbauer, A. Jarmola, and L. Kalvans, Physical Review A **78**, 013417 (2008), ISSN 10941622.

[18] N. Castagna and A. Weis, Phys. Rev. A **84**, 053421 (2011).

[19] E. Breschi and A. Weis, Physical Review A **86**, 053427 (2012).

[20] M. P. Auzinsh, R. S. Ferber, and I. Y. Pirags, Journal of Physics B: Atomic and Molecular Physics **16**, 2759 (1983).

[21] C. Andreeva, S. Cartaleva, L. Petrov, S. M. Saltiel, D. Sarkisyan, T. Varzhapetyan, D. Bloch, and M. Ducloy, Physical Review A **76**, 013837 (2007), arXiv:0706.0837.

[22] G. Alzetta, S. Gozzini, A. Lucchesini, S. Cartaleva, T. Karaulanov, C. Marinelli, and L. Moi, Physical Review A **69**, 063815 (2004).

[23] M. Auzinsh, A. Berzins, R. Ferber, F. Gahbauer, L. Kalvans, A. Mozers, and D. Opalevs, Physical Review A **85**, 033418 (2012).

[24] M. Auzinsh, A. Berzins, R. Ferber, F. Gahbauer, U. Kalnins, L. Kalvans, R. Rundans, and D. Sarkisyan, Phys. Rev. A **91**, 023410 (2015).

[25] K. Blushs and M. Auzinsh, Physical Review A **69**, 063806 (2004).

[26] M. Auzinsh, A. Berzins, R. Ferber, F. Gahbauer, L. Kalvans, A. Mozers, and A. Spiss, Physical Review A **87**, 033412 (2013), URL `http://link.aps.org/doi/10.1103/PhysRevA.87.033412`.

[27] L. Allen and J. H. Eberly, *Optical Resonance and Two Level Atoms* (Wiley, New York, 1975).

[28] N. G. van Kampen, Physics Reports **24**, 171 (1976).

[29] M. Auzinsh and R. Ferber, *Optical Polarization of Molecules* (Cambridge University Press, 2005), ISBN 978-0-521-44346-3.

[30] J. P. Barrat and C. Cohen-Tannoudji, J. Phys. Radium **22**, 443 (1961).

[31] M. I. Dyakonov, Sov. Phys. JETP **200**, 1484 (1965).

[32] M. Auzinsh, R. Ferber, F. Gahbauer, A. Jarmola, and L. Kalvans, Physical Review A **79**, 053404 (2009), ISSN 10941622.

[33] D. A. Steck, *Rubidium 87 D Line Data* (2009), revision 2.1.2, 12 August 2009, URL `http://steck.us/alkalidata`.